Nuclear Physics B143 (1978) 1–39

LARGE ANGLE NEUTRON-PROTON ELASTIC SCATTERING FROM 5 TO 12 GeV/c

J.L. STONE, J.P. CHANOWSKI, H.R. GUSTAFSON and M J. LONGO
Randall Laboratory of Physics, University of Michigan, Ann Arbor, Michigan 48109, USA

S.W. GRAY
Department of Physics, Indiana University, Bloomington, Indiana 47401, USA

Received 8 February 1978
(Revised 13 June 1978)

This paper describes a measurement of the neutron-proton differential cross section made at the Argonne National Laboratory Zero Gradient Synchrotron The differential cross sections, based on about 470 000 events, are presented for 8 different momentum ranges between 4.5 and 12.5 GeV/c The data extend from small angles out to about 145° in the c.m s , corresponding to 0 14 $< -t \lesssim$ 19 (GeV/c)^2 at the highest energies. These results in conjunction with previous np charge-exchange data provide almost complete angular distributions in this momentum range. A detailed comparison of the data with existing pp data and with theoretical predictions is made

1. Introduction

In this paper we present a detailed account of an experiment to measure differential cross sections for neutron-proton elastic scattering between 4.5 and 12.5 GeV/c over a very large range of four-momentum transfers ⋆. The experiment was carried out in a neutron beam at the Argonne National Laboratory Zero Gradient Synchrotron (ZGS). The beam, which had a broad momentum spectrum, was incident on a liquid hydrogen target. A conventional wire spark chamber magnetic spectrometer was used to momentum analyze and measure the scattering angles of the recoil proton. The scattered neutron was detected in an array of wire spark chambers, zinc plates and scintillation counters. All kinematic variables were measured except the momenta of the incident and scattered neutrons so that a two-constraint fit to neutron-proton elastic scattering was possible. The incident neutron momentum for each event was determined from the fit. Six overlapping settings of the proton spectro-

⋆ A brief report of these results and their interpretation appeared in J L Stone et al , Phys Rev Lett 38 (1977) 1315, 1317.

meter and the neutron detector were used to collect data over the entire kinematic range.

In sect. 2 we briefly review existing data on nucleon-nucleon elastic scattering at high energies. Sect. 3 summarizes the theory. In sect. 4 the experimental apparatus is described, and in sect. 5 the data analysis is discussed. The results are presented in sect. 6. In sect. 7 we discuss the results and compare them with theoretical predictions.

2. Summary of previous experimental data

Neutron-proton differential cross sections have been measured at various momenta by several earlier experiments [1–6]. Most previous experimental effort has concentrated on studying either the small-angle diffraction peak or the backward ("charge exchange") peak.

Gibbard et al. [1] made measurements over the momentum range of 5 to 30 GeV/c for $0.2 \lesssim -t \lesssim 1.2$ (GeV/c)^2. These early data showed that the np cross sections at small $|t|$ were similar to proton-proton data.

Two experiments at the CERN Proton Synchrotron [2] and at IHEP Serpukhov, USSR [3] have yielded data extending slightly beyond the diffraction peak in the momentum range of 10 to 70 GeV/c and covering four-momentum transfers of $0.2 < -t \lesssim 2.8$(GeV/c)^2. The scattered neutron was detected in a rather simple detector consisting of an iron converter plate followed by a single multiwire proportional chamber.

The only previous large angle neutron-proton elastic data above 1 GeV/c are those of Perl et al. [4]. These measurements covered several momenta between 2 and 7 GeV/c and extended to scattering angles well beyond 90° in the c.m.s.. The experimental technique was similar to the present experiment except that optical chambers were used in the earlier experiment. The cross sections below 7 GeV/c show little evidence of any structure and vary smoothly with $|t|$.

Neutron-proton charge-exchange cross sections have been measured at high energies by several groups using a variety of experimental techniques [5,6]. Of particular interest here are the data of Miller et al. [5] which were taken in essentially the same neutron beam at the Argonne ZGS that was used for this experiment. They carried out a high-statistics measurement of the np charge-exchange reaction for incident momenta between 3 and 12 GeV/c in 1 GeV/c bins. Their data in conjunction with large-angle np elastic measurements from this experiment yield almost complete angular distributions for the np system in this momentum range.

Proton-proton elastic-scattering data which extend to large angles have been reported by Clyde et al [7], Allaby et al. [8], Kammerud et al. [9] and Ankenbrandt et al. [10], over the momentum range from 3 to 24 GeV/c. Below 7 GeV/c the differential cross sections show no structure and decrease smoothly as $|t|$ increases. Above 7 GeV/c a shoulder appears in the cross sections around $|t| \simeq 1.4$ (GeV/c)^2.

More recent experiments [11] at Fermilab and ISR energies on pp elastic scattering have revealed that the structure at $|t| \approx 1.4\ (\mathrm{GeV}/c)^2$ in low-energy data develops into a pronounced dip above 100 GeV/c. Other recent pp experiments (12) have shown the steepening of the logarithmic slope for $|t| < 0.2\ (\mathrm{GeV}/c)^2$ whose existence was suggested by Carrigan [13]

Experiments by Akerlof et al. [14], Allaby et al. [8] and Kammerud et al. [9] have measured the proton-proton differential cross section at 90° in the c.m.s. as a function of s, the c.m. energy squared. Those data show a power law energy dependence like s^{-n} for $s \gtrsim 8\ \mathrm{GeV}^2$. The data show a deviation from power law behavior when $s < 8\ \mathrm{GeV}^2$. At 90° in the c.m.s. this corresponds to $|t| \lesssim 2.6\ (\mathrm{GeV}/c)^2$. This suggests the onset of a "large-angle regime" when $t \gtrsim 2.6\ (\mathrm{GeV}/c)^2$.

3. Summary of theoretical work

In this section we shall review some of the theoretical work relevant to the elastic scattering of hadrons at high energies. We refer the reader to ref. [15] for a good review of small angle scattering models. Ref. [16] provides a good review of large angle scattering models.

3.1. Constituent models

Experiments measuring deep inelastic lepton-hadron scattering have demonstrated that hadrons have an effective pointlike constituent structure. Thus one expects *intuitively* that hadrons can scatter to large transverse momenta *via* hard, large angle scattering processes involving their constituents. Most constituent models assume that mesons and baryons are composite bound states of 2 or 3 valence quarks and a neutral "sea" of quark-antiquark pairs.

Due to the pointlike nature of the constituents in these models, the structure of the cross section for an exclusive process A + B → C + D is predicted to be

$$\frac{\mathrm{d}\sigma}{\mathrm{d}t}(s,t) \xrightarrow[P_\mathrm{T}^2 >> (\mathrm{masses})^2]{} (P_\mathrm{T}^2)^{-N} F(t/s)\,. \tag{1}$$

This factorization of the cross section into a power times a function of the dimensionless "scaling" parameter, t/s, is called power law scaling. This scaling law also implies a power law fall-off at fixed c.m.s. angles of the form

$$\frac{\mathrm{d}\sigma}{\mathrm{d}t}(s)\bigg|_{\theta^*\,\mathrm{fixed}} \sim s^{-n} f(\theta^*)\,. \tag{2}$$

In the "hard-scattering models" that have been proposed the high transverse momentum reaction is assumed to occur as the result of a *single* large angle scattering a + b → c + d of constituents a and b. Fig. 1 illustrates the underlying structure of

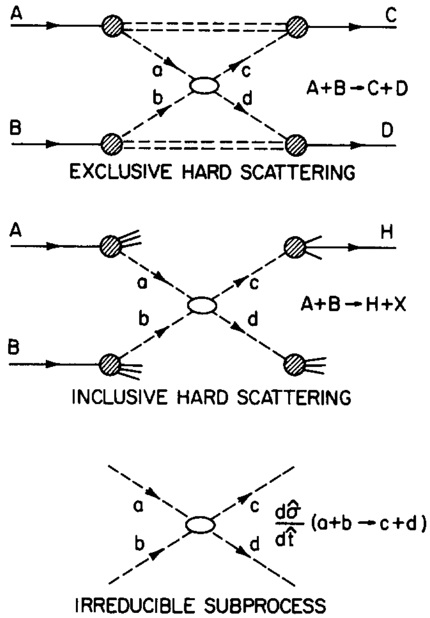

Fig. 1. Diagrams for "hard scattering models" of exclusive and inclusive reactions The underlying subprocess is a single large angle scattering a + b → c + d of constituents a and b

these models for exclusive and inclusive processes. In the figure, the solid lines with arrows represent particles and the dashed lines with arrows represent constituents. For the exclusive scattering process A + B → C + D, constituents a and b undergo a hard scattering and recombine with the other constituents at the outgoing vertex to form the final state particles C and D. For the inclusive process A + B → H + X, the observed high P_T hadron, H, results from the decay or fragmentation of a *single* constituent following a hard scattering. The remainder of the process involves fragmentation of the in- and outgoing particles with small mean transverse momentum. Thus both exclusive and inclusive scattering contain the same irreducible subprocess a + b → c + d Depending on the specific model, the interacting constituents can be quarks, diquarks, or hadrons.

A rather basic mathematical structure based on the naive quark model of hadrons has been suggested by Brodsky and Farrar [17] and independently by Matveev et al. [18], Their objective was to estimate the exponent n for the fixed angle power law-fall-off of the differential cross section given by eq. (2). Their prescription is to count the minimum number of elementary fields, i.e. quarks, leptons and photons, involved in the large angle collision. Hence, for an exclusive process A + B → C + D,

$$n = n_A + n_B + n_C + n_D - 2 ,$$

where n_A, n_B, ..., are the number of elementary fields required to construct particle

A, B, ..., i.e. $n_{\rm nucleon} = 3$, $n_{\rm meson} = 2$ and $n_{\rm lepton} = n_{\rm photon} = 1$. The fixed angle s-dependences of typical hadronic reactions obtained from these dimensional counting rules show remarkable agreement with experiment.

The constituent interchange model (CIM) of Brodsky, Blankenbecler and Gunion (BBG) [19] assumes specific mechanisms for the irreducible subprocess in which the hard scattering takes place. For exclusive reactions the dominant subprocesses are taken to be quark exchange and quark interchange The CIM is attractive because it automatically satisfies the constraints of analyticity and crossing behavior and leads to a smooth connection to the usual Regge phenomenology at small $|t|$ and $|u|$. A simple version of the model treats the nucleon like a bound state between a quark and a di-quark core of spin-1. Then the cross section is

$$\frac{d\sigma}{dt}(\mathrm{NN} \to \mathrm{NN}) \sim s^{-12}\,\frac{J(\sin\theta)}{(\sin\theta)^{12}}\,, \tag{3}$$

where $J(\sin\theta)$ is a slowly varying function. The power of s is -12 in this model, different from -10 given by the dimensional counting rule. Some would argue that 90° proton-proton data in fact exhibit an s^{-12} dependence when $s > 30$ GeV^2.

Another investigation of large angle scattering has been conducted by Preparata [20] within the framework of a massive quark model (MQM). In this model the fundamental constituents are quarks with very large mass.

In a different interpretation of constituent models Fishbane and Quigg [21] have discussed the ratios of cross sections at 90° in the c.m.s. Their assumption is that the cross sections for the reaction A + B → C + D at large angles is proportional to the number of distinct ways the constituents of A and B can be recombined to form C and D. The usual quark model assignments of quarks are used. They predict the ratio of np to pp differential cross sections at 90° to be $\frac{3}{4}$. This result is compared with our data in sect. 7.

In addition to the models discussed above, various authors have suggested parameterizations of the nucleon-nucleon elastic scattering data.

Landshoff and Polkinghorne [22] have published an empirical fit to large angle proton-proton elastic data at intermediate energies ($15 \leqslant s \leqslant 60$ GeV^2) and $-t \gtrsim 2.5$ (GeV/c)^2. Their result is

$$\frac{d\sigma}{dt}(\mathrm{pp} \to \mathrm{pp}) \sim s^{-9.7}(\sin\theta^*)^{-14}\,. \tag{4}$$

Pire [23], assuming the validity of the dimensional counting rules and working in the framework of the CIM, has attempted to derive the angular dependence of large angle baryon-baryon scattering. For the neutron-proton reaction, the result is

$$\frac{d\sigma}{dt}(\mathrm{np} \to \mathrm{np}) = \frac{d\sigma}{dt}(\mathrm{np})\Big|_{90^\circ}(1 - \cos^2\theta^*)^{-4}\,.$$

Hojvat and Orear [24] have fit recent proton-proton data from the ISR and suggest that

$$\frac{d\sigma}{dt}(pp \to pp) = A e^{-7P_T}$$

for $s > 300\ \mathrm{GeV}^2$ and $P_T > 1.5\ \mathrm{GeV}/c$. They claim that the same exponential fits lower energy data, $10 < s < 60\ \mathrm{GeV}^2$, if A is a slowly decreasing function of s, i e. $A = s^{-2}$ This result gives a fixed angle energy dependence of $s^{-6\ 6}$ It should be noted that although the ISR data is at high P_T, the c.m s scattering angle is $\theta^* \simeq 4.85°$

In another parameterization for proton-proton elastic scattering, Gotsman [25] has suggested that the fundamental length scale of the CIM be $(P_T)^{-1}$ rather than $s^{-1/2}$ as is usually done. This leads to a "non-factorizable" form of the scattering amplitude and to

$$\frac{d\sigma}{dt}(pp \to pp) \sim s^{-2}(P_T^2 + m_V^2)^{-8}$$

for $15 \leqslant s \leqslant 60\ \mathrm{GeV}^2$, where $m_V^2 = 0\ 71\ \mathrm{GeV}^2$ represents a typical mass scale.

3.2. Other models

We now turn our attention to models which attempt to explain high P_T phenomena without invoking quark-like structureless constituents.

One such attempt is the statistical model suggested by Fermi, by Fast, Hagedorn and Jones [26] and others and later discussed by Frautschi [27] and Eilam [28]. This model makes a prediction that with increasing energy the cross section at 90° should fall exponentially in P_T. It also predicts that the neutron-proton and proton-proton cross sections should be equal and symmetric about 90° in the c.m.s.

Wu and Yang [29] make a prediction about large-angle scattering in a "random phase" isotopic-spin model. The assumption is that elastic differential cross sections in different isotopic-spin channels have the same absolute isosopin amplitudes and random relative phases. Wu and Yang predict the ratio

$$R = \frac{\frac{d\sigma}{dt}(np \to np)}{\frac{d\sigma}{dt}(pp \to pp)} = \frac{1}{2} \tag{5}$$

at large angles, e.g. 90° in the c.m.s.

At this point we also note that charge independence within the context of isospin symmetry requires that [30]

$$\left.\frac{d\sigma}{dt}(np)\right|_{90°} \geqslant \left.\frac{1}{4}\frac{d\sigma}{dt}(pp)\right|_{90°}$$

4. Experimental details

A general layout of the experimental area is shown in fig. 2. A well collimated neutron beam is passed through a liquid hydrogen target. The momentum and angle of the recoil proton were measured by a wire chamber magnetic spectrometer. The scattered neutron trajectory was determined by locating the conversion point in the neutron detector and then connecting this point to the midpoint of the proton trajectory extrapolated into the liquid hydrogen target. Both the proton spectrometer and neutron detector were rotated into various settings so that data were collected over a wide kinematic range. Numerous veto counters (A1–A9), not all shown in fig. 2, reduced the trigger rate from inelastic interactions. A detailed description follows.

4.1. Neutron beam

A detailed layout of the neutron beam is shown in fig. 3. The neutron beam was produced by steering the circulating proton beam of the ZGS onto an internal beryllium target. Three different production angles with respect to the circulating proton beam, 0.5°, 2.0° and 3.5°, were used in the course of the experiment. Since the spec trum of neutron momenta in the beam is strongly dependent upon the production angle, cross sections were determined for each spectrum separately and then combined for the final cross section.

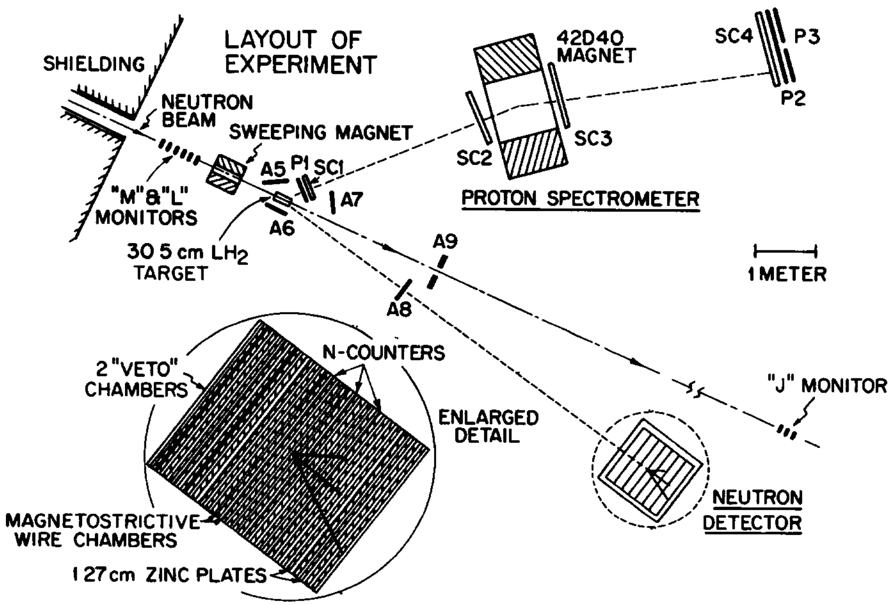

Fig. 2. Layout of the apparatus.

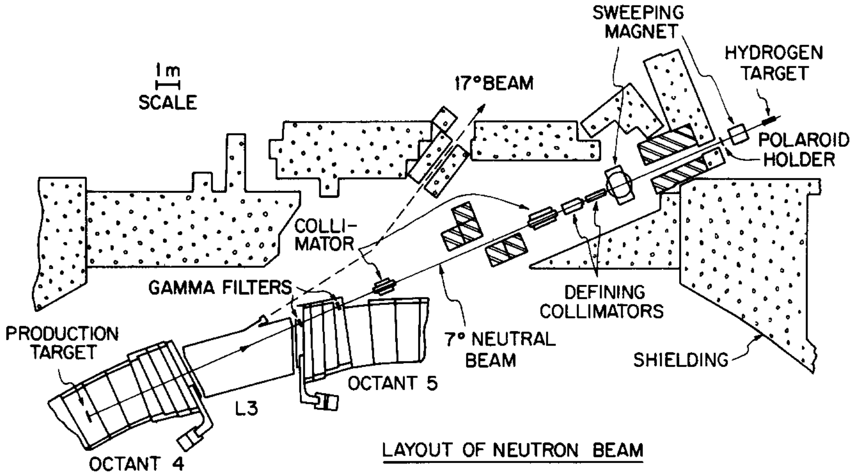

Fig. 3 Layout of the neutron beam line

Charged particles were swept from the beam by the 19.8 kG magnetic field of the ZGS, then by a sweeping magnet downstream of the defining collimators and finally by a pitching magnet immediately upstream of the hydrogen target 99% of the γ's in the beam were removed by two lead filters with a total thickness of 2.54 cm, equivalent to 4.5 radiation lengths. Other possible neutral contaminations in the beam were K^0's and $\bar{n}$'s. However, both contaminations were estimated from production data to be $< 1\%$.

Beam halo was reduced by a non-defining collimator about 12 m downstream of the Be target Two circular brass defining collimators with a total length of 2 m were located about 25 m from the Be target. Immediately downstream of these were two rectangular brass clipping blocks each 0.91 m long which limited the horizontal width of the beam. The collimated beam had a spot size at the hydrogen target of 2.54 cm in width and 4.45 cm in height with negligible halo.

At the maximum ZGS proton momentum of 12 5 GeV/c and average intensity of 2.5×10^{12} protons per accelerator pulse, a neutron beam flux of about 3×10^6 neutrons was attained over a spill length of about 550 ms

The relative intensity of the neutron beam was monitored by 3 sets of monitor counters labeled M, J, and L in fig 2. Each set consisted of three small scintillation counters positioned one behind the other and separated by about 5 cm. The first counter of each set was used as a veto counter so that the monitors countered neutrons which converted in a 0 6 cm piece of lucite placed in front of the second counter and formed charged particles that could be detected by a coincidence between the second and third counters. Counts from each monitor were scaled and assumed to be proportional to incident neutron beam flux.

Throughout the experiment, ratios of these monitors were watched carefully to insure their consistency while data taking was in progress. These ratios typically tracked to within 2%. The monitor data were used in the analysis to relatively normalize data taken at various settings of the apparatus

4.2 Liquid hydrogen target and veto counters

The liquid hydrogen target assembly was chosen so that there would be a minimum amount of material for particles to pass through for 90° on either side of the beamline. The flask was a cylinder made of 127 μm mylar, 5.08 cm in diameter and 30 5 cm long. For thermal insulation the flask was wrapped with 12 layers of 6 μm aluminized mylar. The target flask was enclosed in a cylindrical vacuum chamber with 889 μm aluminum walls which was sealed with a 254 μm mylar film. The ends of the aluminum casing had beam entrance and exit windows of 127 μm mylar.

Throughout the experiment data runs were taken with the target empty but with all other experimental conditions the same as for normal data runs. These target empty runs served as a measure of the number of background events originating from sources other than the liquid hydrogen. It was found that target empty sources produced a negligible background (<1 0%).

Numerous veto counters were used in this experiment to help identify the correct event topology before triggering the spark chambers. Some of the 9 veto counters are shown in fig. 2. The target was surrounded as completely as possible by veto counters. Except for A8, each of these counters were constructed from two pieces of scintillator separated by a sheet of lead. These counters were sensitive to low and high energy charged particles and to gamma rays coming from the target. Since an accidental count from the veto counters could veto a good event, the accidental veto rate was measured by comparing $L[\bar{A}]$ coincidences with L coincidences where L is one of the monitor telescopes described above and $[\bar{A}]$ represents an anticoincidence with the summed veto counters purposely mistimed with respect to the L counters.

4.3. Neutron detector

The neutron detector consisted of an array of 30 wire spark chambers, 28 zinc plates and 6 scintillation counters sandwiched together as shown in fig. 4. These were divided into 7 modules, each composed of 4 chambers and 4 zinc plates Each module was separated by a scintillation counter. In addition, there were 2 "veto" chambers immediately preceding the first module. Not observing a track in these veto chambers helped insure that the incoming particle was neutral. Each chamber had a set of horizontal and a set of vertical aluminum wires spaced 1 mm apart. The wire planes were separated by a 1.27 cm gap. The dimensions of the active volume of the detector were 86.4 cm wide, 50.8 cm high, and 105 cm deep A mixture of 90% Ne and 10% He with a slight admixture of ethyl alcohol was maintained in the chambers and was recirculated *via* a gas recirculation and purification system. A 125

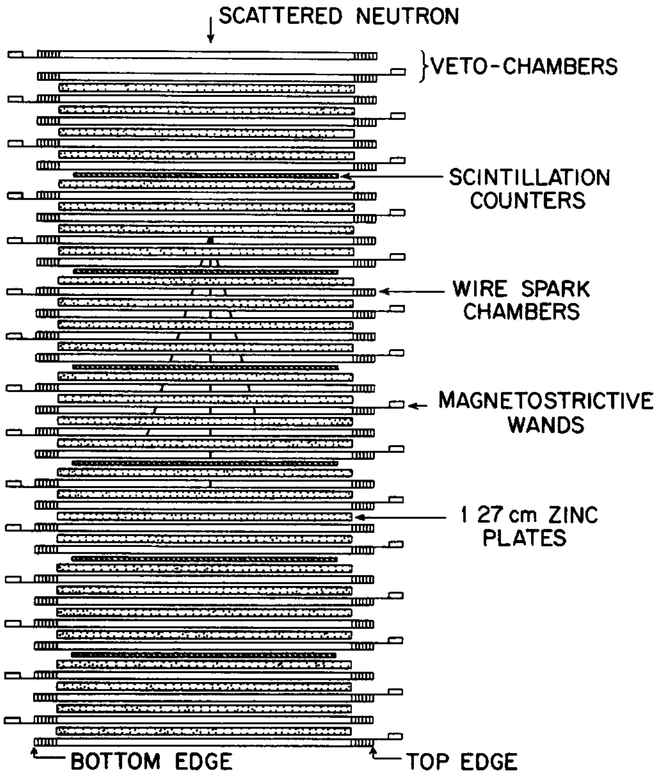

Fig 4. Side view of the neutron detector

V d.c. clearing voltage was kept across the chambers at all times Each chamber was powered by a 6300 pf capacitor charged to about 14.5 kV. Upon receipt of an event trigger the capacitors were connected across the chamber planes through spark gaps. Fiducials at each chamber edge were pulsed in parallel with the chambers. Coordinates of sparks and fiducials were recorded on "static type" magnetostrictive readout which made use of the permanent magnetization induced on the magnetostrictive lines by the currents in the struck wires [31].

The performance of the chambers was monitored online with a Hewlett Packard 2115 computer which continuously checked for problems. A scope display of all sparks and fiducials from both views was generated online for each event and could be examined by the experimenters at any time. Fig. 5 shows examples of this computer display for typical high, intermediate, and low energy neutron induced showers. In the figure the horizontal and vertical views are delineated by fiducial sparks The solid vertical lines represent scintillation counters which were triggered by the shower. The incoming neutron enters from the left

The 6 neutron counters were made of Pilot B scintillator and were viewed by

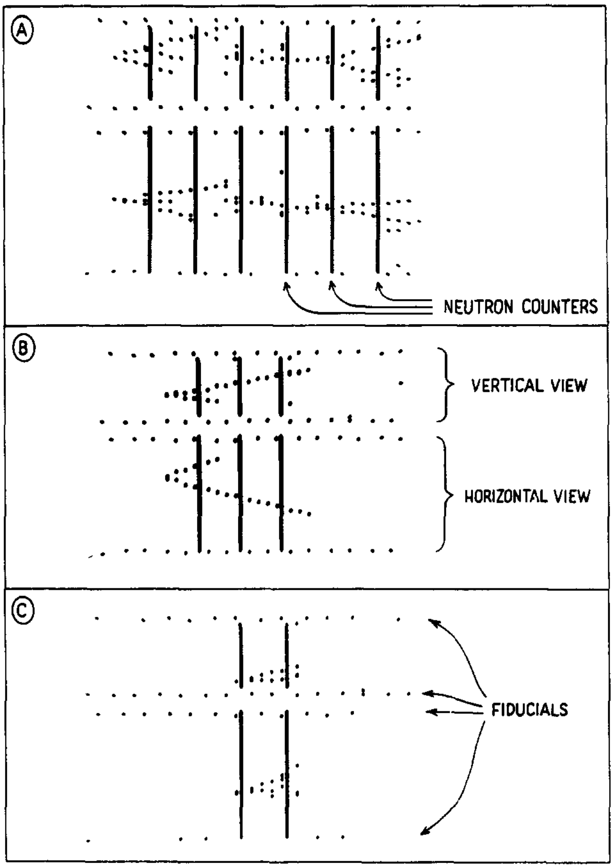

Fig 5. Computer displays of typical neutron showers (A) high energy, (B) intermediate energy, and (C) low energy Neutrons are incident from the left

RCA 6810A photomultiplier tubes. The scintillator dimensions were 1 cm × 84 cm × 46 cm. The event trigger required a coincidence between any two of the six counters. The counters which fired for each event were recorded by the computer as part of the shower data.

Neutrons which entered the detector and interacted in the zinc plates produced electromagnetic and hadronic showers of charged particles. Each of the 28 zinc plates was 1.27 cm thick. A total of 185 g/cm^2 of zinc and scintillator provided 1.4 collision lengths to give a neutron conversion efficiency of 75%. For each event, x and y coordinates for up to 8 sparks in each gap were recorded as well as the scintillation counters which detected the shower A computer program was written to sort out the shower information and to determine the point of conversion of the incoming neutron. The scattering angles of the neutron are obtained when the vertex is connected to the liquid hydrogen target where the neutrons originate. The algorithm used to determine the location of the neutron vertex in the detector is described in subsect. 5.3.

4.4. Proton spectrometer

The proton spectrometer consisted of 4 sets of wire spark chambers, an analyzing magnet, and 3 trigger counters as shown in fig. 6. Two sets of chambers were loca-

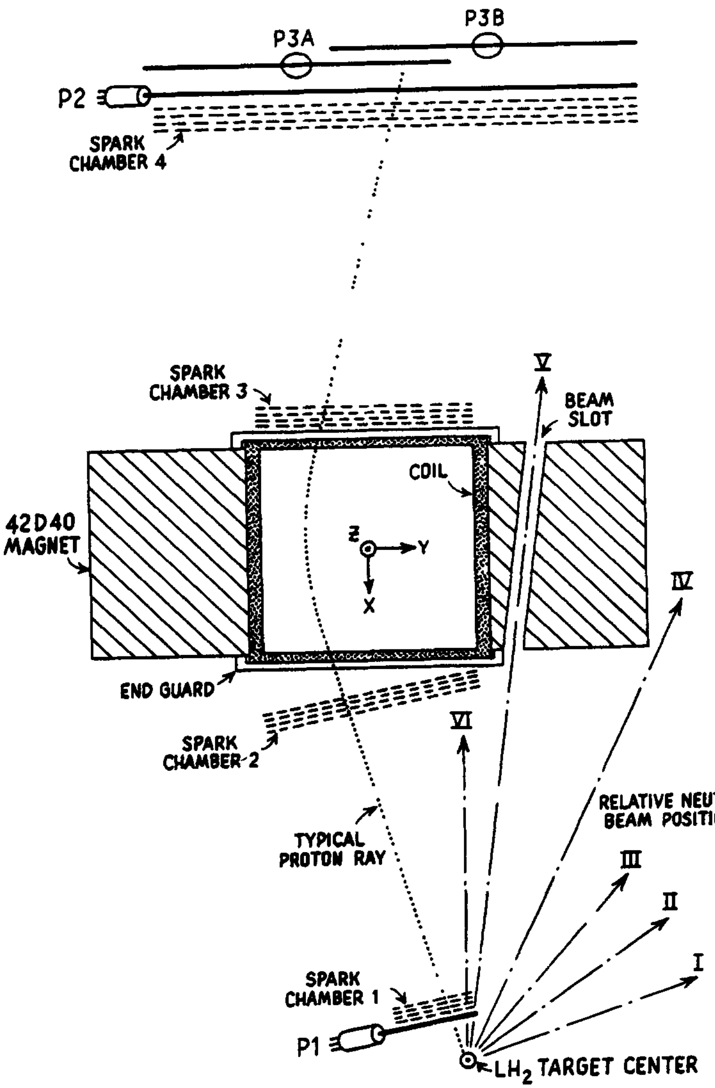

Fig. 6. The proton spectrometer and the relative positions of the neutron beam for the 6 experimental arrangements.

ted on each side of the magnet and were separated by 1.5 m. All the chambers and counters were hung from two 8-inch aluminum channel beams. The entire spectrometer could move as a single unit with multiton rollers To cover the desired kinematic range it was necessary to use 6 different arrangements of the proton spectrometer and neutron detector. The spectrometer was moved about the liquid hydrogen target as a unit to achieve these settings. The Roman numerals I–VI in fig. 6 show the direction of the incident neutron beam relative to the spectrometer for each setting. For the largest $|t|$ setting where the recoil protons scatter nearly forward it was necessary for the neutron beam to pass through the magnet gap and all the spark chambers in the proton spectrometer.

The analyzing magnet was a 35 ton dipole H-type magnet with pole tips 1.07 m wide and 1.02 m deep with an aperture of 15.2 cm. The magnet was operated with a field integral of 13.6 kG · m for the small $|t|$ settings and 23.7 kG · m for the large $|t|$ settings. The field polarity was such that positive particles would bend toward the incident beam direction. Since larger angle protons have lower momenta, this tended to recombine low and high momenta. The field strength was monitored continuously by a digital voltmeter connected across a calibrated shunt resistor in the magnet current supply line. End guards surrounding the magnet aperture reduced the fringe field to $\lesssim$ 50 gauss in the regions of the second and third spark chamber sets. The magnetic field was mapped by our group using a Rawson probe. Readings were taken on a 1″ grid over the entire magnet aperture. These were normalized to measurements taken at the center of the magnet with an NMR probe against which the digital voltmeter and shunt were calibrated. The field was found to be very uniform with deviations occurring only near the edges of the pole tips.

The spectrometer used 4 modules of wire spark chambers. Each module consisted of four planes of 0.18 mm diameter aluminum wires spaced 1 mm apart. The wire orientations for the first three chamber modules were x–y–u–v and were x–y–y–x for the last module. The x–y orientation corresponded to horizontal and vertical wires. The u–v wires were orthogonal but rotated 45° relative to the x–y planes.

The same Ne-He-alcohol mixture used in the neutron chambers was circulated through the proton chambers. A 90 V d.c. clearing voltage was kept across the chambers et all times. The proton chambers used a conventional prompt magnetostrictive readout with 2 SAC scalers assigned to each plane. Relative alignment of the chamber modules was achieved using survey data and "straight tracks" recorded with the bending magnet off. Times-of-flight for P1-P2 and P1-P3A/P3B were recorded as part of the event data.

4.5. *Logic and data acquisition*

The event trigger was a fast coincidence of $PN\bar{A}$ where P is a coincidence of P1P2P3, N is a coincidence between any two of the 6 neutron counters, and $\bar{A}$ is the passive sum of the 9 veto counters. When this requirement was met, a signal was sent to electronics which initated the spark chamber triggering sequence. Simultaneously, a signal was sent to interrupt the HP-2115 computer which initiated the data acquisition sequence.

All logic modules were gated on only during beam spills. The computer also gated off the system for about 100 ms per event while data acquisition was in progress. A lucite Čerenkov counter inside the accelerator enclosure provided a signal proportional to the instantaneous beam intensity. This signal was used to shut the experiment off during spikes in the beam spill.

The neutron spark chambers used a "static" magnetostrictive readout [31]. Thus, the computer had to interrogate each of the 30 neutron chambers individually by sending an address and strobe signal to an "interrogator" box. The interrogator pulsed the specified wand and the SAC scalers clocked the propagation times for up to 8 sparks. The computer then read the scalers and proceeded to sequentially interrogate all 30 chambers. After storing data for about 10 events in a memory buffer the HP-2115 wrote a data record on magnetic tape.

The monitors and various scaled coincidences were recorded on both CAMAC blind scalers and TSI scalers. The CAMAC scalers were read and written on magnetic tape with each data record.

5. Data analysis

The general scheme of the data analysis is as follows. The raw data tapes were processed by a reconstruction program which was run offline on a PDP-10 computer. This program extracted the scattering angles and momenta of the recoil proton from the raw spectrometer data. Next the angles of the scattered neutron were determined by analyzing the shower data from the neutron detector. The incident neutron beam angles, measured from Polaroid films exposed in the beam, were submitted to the program *via* cards. These measured kinematic variables were fitted to the hypothesis that the event was $n + p \to n + p$ by a least-squares kinematic fitting program. The fit calculated the unmeasured momenta and a chi-squared, χ^2, for each event. Events with low χ^2, typically less than 10, were considered to be the desired elastic events. The geometric detection efficiencies were calculated by a Monte Carlo program and the neutron detection efficiencies were extracted from a separate set of measurements. The output of the reconstruction program and the efficiencies were submitted to a program which calculated np differential cross sections. Various corrections were made and the cross sections were normalized by using the optical theorem. The various phases of the analysis procedure will be elaborated upon below.

5.1. Proton trajectory and momentum

The first phase of the analysis procedure involved finding the scattering angles and momenta of the recoil proton from the raw spectrometer data. Two spark chamber sets in front of the analyzing magnet were used to determine the proton scattering angles θ_p and φ_p. The bend angle through the magnet was determined in part by two spark chamber sets behind the magnet. The proton momentum, P_p, was calculated from the bend angle and the magnetic field integral. (A detailed description of this procedure can be found in ref. [32].) The calculated momentum was corrected for momentum lost by the proton in traversing the hydrogen target and the upstream half of the spectrometer.

Because of background or accidental tracks in the spectrometer it was possible for more than one set of sparks in each of the 4 chamber sets to give an acceptable fit. This situation yielded several possible proton trajectories. Most of the time only one "good" track was found, however, when there were two or more, all were submitted to the kinematic fitting program which is described below. Of the elastic events, $\lesssim 8\%$ came from events with $\geqslant 2$ proton tracks.

5.2. *Neutron vertex determination*

In the next phase of the analysis procedure the angles of the scattered neutron, θ_n and φ_n, were determined. This was done by locating the conversion point (vertex) of the neutron induced shower in the neutron detector and then connecting it to the midpoint of the proton trajectory extrapolated into the liquid hydrogen target.

The neutron vertex position determination is a pattern recognition problem. The showers that develop in the neutron detector have various topologies and depend strongly on the neutron energy. A computer display of typical high, intermediate, and low energy showers is shown in fig. 5. The showers can range from short tracks with few sparks at low energy to extensive tracks with numerous secondary interactions which fill the entire detector at higher energies. Also, the showers occasionally show wide-angle and backward tracks and in some cases there are no distinguishable tracks at all, just scattered sparks.

Two basic methods were used in locating the desired conversion point. First, it was assumed that the most energetic charged tracks should be the longest and most forward going with respect to the incident neutron. Therefore, straight trajectories emanating from a common point were sought in the shower data. Appearance of these trajectories in both views and intersections of two or more trajectories gave good candidates for the conversion point or vertex. Secondly, since some showers showed no straight tracks, either because of the very high multiplicity of sparks or because of very few sparks, a second method was to find the center of gravity of all sparks and to take the nearest cluster of sparks as a vertex candidate.

Since the cross section to be measured does not depend on the total efficiency but only on the momentum dependence of the efficiency, criteria could be imposed to improve the accuracy of the neutron vertex determination. A minimum of 3 sparks in each view were required before a vertex search was attempted. Only sparks which were associated with latched neutron counters were considered in the search. To minimize confusion arising from wide angle or back scatters, tracks with angles greater than 45° relative to the detector coordinate axes were eliminated. Any track which appeared in the two veto chambers preceding the first zinc plate could have been from a charged rather than neutral particle entering the detector and thus was ignored. Vertex candidates appearing near the edges of the detector were eliminated because portions of the showers could have been lost out the edges resulting in a poor vertex determination. If any of these criteria were not met, the vertex was eliminated. Up to six possible vertices were allowed for each event Based on the total number of sparks in a cone emanating from the vertex, the program chose the 2 most likely vertices for submission to the fitting program.

The success of the VERTEX program was evaluated by looking at the spatial resolution of the neutron vertex determination. Based upon proton kinematics alone, it was possible to choose an almost pure sample of np elastic events when the apparatus was set at the lowest $|t|$ position. By imposing the coplanarity constraint for elastic scattering on this sample of events, the plane defined by the recoil proton and the incident neutron was projected onto the neutron detector. The perpendicular distance of the vertex from this plane is plotted as the neutron spatial resolution in fig. 7. The FWHM is 1.5 mm with few events falling outside ±2.0 mm.

The efficiency of the VERTEX program for finding vertices as described below is 88%. The efficiency for converting a neutron in the detector is about 75%. Hence,

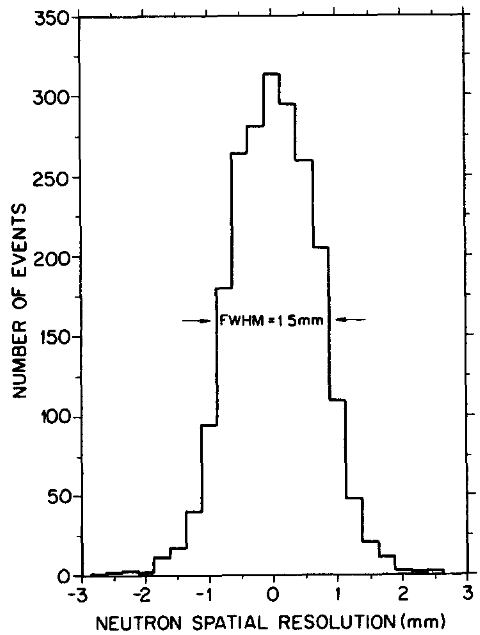

Fig. 7. Distribution of vertical distances of neutron vertices from the position predicted from the coplanarity requirement.

the overall neutron detection efficiency is the product of these two efficiencies and is approximately 65%. The momentum dependence of the detection efficiency is discussed below.

5.3 Kinematic fitting and selection of elastic events

In the next phase of the analysis, the measured values of the kinematic variables and their estimated errors were fitted to the elastic scattering hypothesis to obtain an optimum solution. Since the only unknown quantities were the incident and scattered neutron momenta, a 2-C fit was performed. The fitting technique was a standard least-squares analysis in which Lagrange multipliers are used to impose the kinematic constraints of energy and momentum conservation. The measured quantities were adjusted by the least-squares method until a solution was obtained for which χ^2 was a minimum and all the constraints were satisfied. It was assumed that the errors in the measured quantities were uncorrelated to first order.

The selection of elastic events was based on the value of χ^2 In the case where multiple proton trajectories or neutron vertices were submitted to the fitting program, the combination with the best χ^2 was used. Typically events with $\chi^2 < 10$ were considered to be elastic. It was assumed that for $\chi^2 \lesssim 20$ background events from inelastic reactions were uniformly distributed in χ^2. Therefore, the region $10 < \chi^2 < 20$ was taken to represent the background contamination under the χ^2 peak. These background events were subtracted from the number of elastic events. Since the level of background was a function of $|t|$ and P, this correction was determined separately for each P-t bin.

A low χ^2 was the only criterion applied to select elastic events. At small $|t|$ approximately 88% of the total triggers were elastic events, whereas at large $|t|$ only about 0.5% were elastic.

5.4. Geometric detection efficiency

In a separate phase of the analysis the geometric acceptance of the experimental apparatus was determined by Monte Carlo techniques. The probability of observing an elastic event for a given incident momentum, P, and four-momentum transfer squared, t, was called the geometric detection efficiency. Every event was weighted by this probability in the cross section calculation.

The Monte Carlo program simulated a large number of elastic events and calculated efficiencies for an array of points in P and t extending over the kinematic range of the data. All parameters which could vary randomly in the data were randomly generated in the program. The same criteria used to reject events in the reconstruction program were also used in the Monte Carlo program.

A number of checks were performed to insure that the Monte Carlo program was operating consistently with the event reconstruction program. One such check compared the distributions of sparks in the chambers from reconstructed elastic events with spark distributions generated by the Monte Carlo. In another check events generated by the Monte Carlo program were analyzed by the reconstruction program and the results compared. All checks indicated that the two programs were operating consistently.

5.5. Momentum dependence of the neutron detection efficiency

The scattered neutrons in this experiment ranged in momenta from about 1 GeV/c up to about 12 GeV/c. Thus it was necessary to measure the momentum dependence for detection of these neutrons. The procedure for doing this was based on the fact that protons coming off near 90° in the lab system can only come from elastic scatterings.

The apparatus was set up at small $|t|$, where the triggers were mostly elastic events, and the neutron counter requirement was removed from the event trigger logic. All chambers, including the neutron chambers, were fired by a coincidence between the proton counters with no veto pulse. About 73K events were taken with this $P\bar{A}$ trigger. Cuts were made on the proton angle and momentum to distinguish protons from elastic events from those from inelastic events. When the neutron beam contained neutrons with momenta up to 12 GeV/c it was not possible to obtain a pure sample of elastic events for incident neutron momenta below 6 GeV/c. Thus, arrangements were made to run the ZGS for a shift with a peak momentum of 6.95 GeV/c to extend the detection efficiency measurements below 6 GeV/c.

Given the scattering angles and momentum of the recoil proton and the angles of the incident neutron, a zero constraint kinematics calculation yields all other unknown kinematic parameters, *viz*, the momenta of the incident and scattered neutrons and the angles of the scattered neutron. If the predicted angles of the scattered neutron fell well within the limits of the neutron detector, then a neutron shower could be "expected" in the neutron detector. These "expected showers" were binned *versus* the momentum of the neutron. Events were binned as "observed" when a neutron was found by the VERTEX program and the normal 2-C fitting program gave a low χ^2 for np elastic scattering. In this fit, all criteria were the same as for the regular data, including a minimum of two neutron counter "latches". The ratio of the number of neutron showers "observed" to those "expected" is the detection efficiency.

Finally, the momentum dependence of the neutron detection efficiency determined by this calibration is plotted in fig. 8. The theoretical maximum efficiency is just the probability of a neutron interacting inelastically in the detector. The theoretical zero efficiency occurs when a recoil proton with energy equal to that of the neutron has a range too small to meet the two neutron counter requirement for a trigger.

While running the ZGS at 6.95 GeV/c some data were also taken with the normal $NP\bar{A}$ trigger. Thus the momentum dependence of the vertex finding method was obtained by analyzing these $NP\bar{A}$ events in exactly the same manner used to deter-

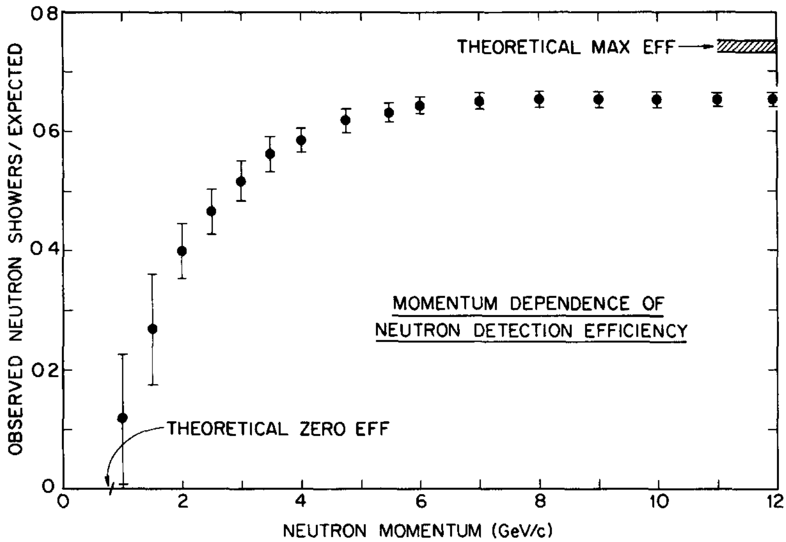

Fig. 8. Neutron detection efficiency *versus* neutron momentum

mine the total detection efficiency. This follows because inclusion of the neutron counters in the trigger effectively removes the conversion efficiency factor from the total efficiency. It was found that the efficiency of the VERTEX program was flat at 88% down to about 3 GeV/c and then fell to 50% at about 1 GeV/c.

5.6. Cross sections and corrections

Cross sections were calculated for the sample of elastic events by weighting the number of events in each P-t interval by the detection efficiencies and the beam monitor data. The geometric detection efficiency and the neutron detection efficiency were calculated for each event by interpolating in tables supplied to the program. Events were rejected for which the probability of being detected was less than 40% of the maximum value for the setting since for low efficiencies the Monte Carlo calculation becomes less reliable.

The uncertainty in the cross section values was calculated from the sum in quadrature of the statistical uncertainty, the uncertainty in the neutron detection efficiency, and a 2% uncertainty assigned to the geometric detection efficiency.

Various corrections have been made to the final cross sections. It was found that the target empty correction was completely negligible. The corrections for inelastic background amounted to less than 20% in the large-angle and backward regions, and less than 10% in the forward region. As explained above, it was assumed that the background events have a flat distribution in χ^2 for $\chi^2 \lesssim 20$.

An additional correction was applied to the cross section to account for protons lost because of nuclear absorption in the target and spectrometer. This was done by a program which uses the optical model to calculate nuclear total cross sections to an accuracy of (5–10)%. The uncertainty introduced into the cross section by this correction was <0.5%.

Studies of the experimental resolutions showed that the uncertainty in incident momentum, P, was dependent on both P and $|t|$. At small $|t|$ and large P the uncertainty in the incident neutron momentum is on the order of the cross-section bin sizes. Hence, an additional correction to the cross sections was necessary to account for the t-dependence of this error. This correction was necessary only for the 11 and 12 GeV/c bins.

5.7. Normalizations

Since data were taken at several settings of the apparatus it was necessary to normalize these data sets relative to each other. This was accomplished by the use of 3 counter telescopes which monitored the incident neutron beam flux. The cross sections from each setting were weighted by the monitor counts from that setting, thus providing a relative normalization between settings. To check this, a comparison of the cross sections in the region where successive settings overlapped was made The normalization of the overlapping points agree within the quoted errors.

There was no way to do an absolute normalization internal to this experiment since the absolute number of neutrons in the beam and their momentum distribution were unknown. However, the optical theorem which relates the imaginary part of the forward amplitude to the total cross section provides a convenient method of obtaining the absolute normalization. For each incident momentum range, the data

Table 1
Parameters used for the absolute normalization

P (GeV/c)	ρ	σ_{total} (mb)	$\left.\frac{d\sigma}{dt}\right\|_{t=0}$ (mb/(GeV/c^2))
4.0	−0 50	43.64	121.64
5.0	−0.4875	41.69	109 89
6.0	−0.475	40 77	104 08
7.0	−0 4625	40.25	100.48
8 0	−0.45	39.92	97.92
9.0	−0 4375	39.70	95.92
10 0	−0.425	39 53	94 25
11.0	−0.4125	39.40	92.81
12.0	−0.40	39 30	91 52

$$\left.\frac{d\sigma}{dt}\right|_{t=0} = \frac{1}{16\pi}\sigma_T^2(1+\rho^2)$$

were fitted to

$$\frac{d\sigma}{dt} = A \exp(B|t| + C|t|^2)$$

for $|t| < 0.8(\mathrm{GeV}/c)^2$. This fit was extrapolated to $|t| = 0$ and the intercept was adjusted to the optical theorem point given by

$$\left.\frac{d\sigma}{dt}\right|_{t=0} = \frac{1}{16\pi}\sigma_T^2(1+\rho^2)\,.$$

The values of σ_T used were calculated from a fit to np total cross-section data given by Murthy et al. [33]. The ratio of the real to imaginary part of the forward scattering amplitude, ρ, was assumed to vary linearly with momentum with ρ equal to -0.5 at 4 GeV/c and -0.4 at 12 GeV/c [34]. Table 1 gives the values of σ_T and ρ used for normalizing the data and the corresponding $d\sigma/dt|_{t=0}$. The uncertainty in this normalization is primarily due to uncertainties in σ_T and ρ and is estimated to be ±10%.

6. Results

The differential cross sections measured in this experiment are presented in fig. 9 and are tabulated in tables 2–9. The data are plotted as $d\sigma/dt$ *versus* $|t|$ in units of mb/(GeV/c)^2. The eight incident momentum bins are 1 GeV/c in width and the value given is that of the center of the bin. The t-bins at small $|t|$ were chosen to be roughly equivalent to the experimental resolution in order to obtain maximum detail. At larger $|t|$, the t-bins were increased in width to maintain approximately the same statistical error from point-to-point. The position of 90° in the c.m.s. is indicated by the ↑ for each momentum bin.

The errors plotted in fig. 9 and listed in the data tables include statistical as well as the point-to-point systematic errors. However, the uncertainty arising from the overall normalization of the data, which is estimated to be ±10% for each momentum bin, has *not* been included in the quoted errors. The point-to-point systematics arise from a number of sources. The uncertainty introduced by the background subtraction contributed typically a 1% error at small $|t|$ and increased to about 10% at large $|t|$. The uncertainty in the geometric acceptance of the detectors as calculated by a Monte Carlo program produced a 2% error for each point. The error introduced by the uncertainty in the neutron detection efficiency was about 1% for scattered neutrons with momenta above 5 GeV/c and increased to about 10% for neutrons with momenta less than 2 GeV/c. An error of at most 0.5% resulted in correcting for the nuclear absorption of slow protons in the spectrometer. The uncertainty in unfolding the neutron beam spectrum contributed an error of less than 1% for points with $-t < 2.0$ (GeV/c)^2 in the 11 and 12 GeV/c momentum bins and was negligible

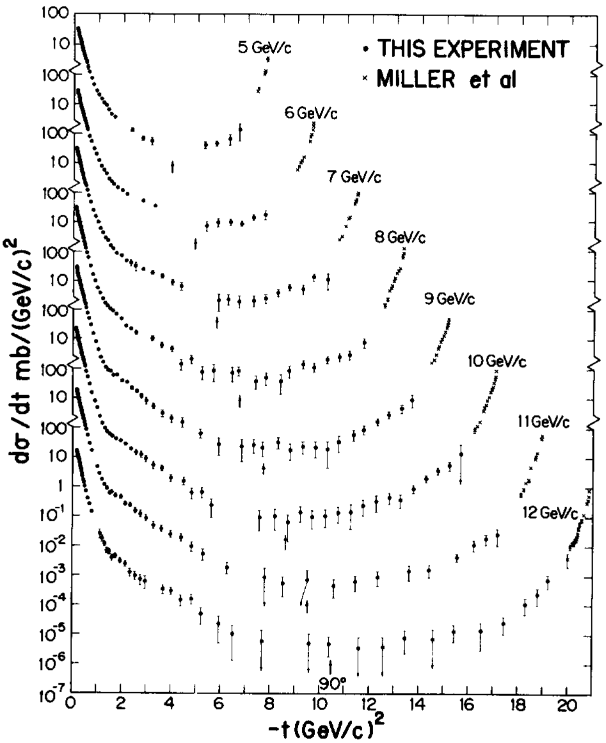

Fig. 9. Neutron-proton elastic differential cross sections for 8 incident momenta from 5 to 12 GeV/c. The ↑ indicates the position of 90° in the c.m s.

at lower momenta. All of these errors were combined in quadrature with the statistical error to yield the quoted errors.

The general features exhibited by the cross sections are as follows. There is a nearly exponential diffraction peak which shows shrinkage with increasing energy. The cross sections fall more slowly as $|t|$ increases and eventually flatten, with a minimum near 90° in the c.m.s. In the backward direction the cross sections rise monotonically and join smoothly with the charge-exchange data of Miller et al. [5]. The large angle data show a steep energy dependence with the 90° cross sections falling by three orders of magnitude between 5 and 12 GeV/c.

The small $|t|$ cross sections are plotted on an expanded scale for $|t| \leqslant 2.0$ (GeV/c)^2 in figs. 10 and 11. There is evidence for a steepening of the logarithmic slope for $|t| \lesssim 0.18$ (GeV/c)^2. This has been observed in pp data from SLAC at 10.4 GeV/c (12). Beyond the small $|t|$ structure the logarithmic slope decreases smoothly as $|t|$ increases with no additional structure for incident momenta less than or equal to 7 GeV/c. At 8 GeV/c there is a hint that structure is developing near $|t| \simeq 1$ 5

Table 2
Dıfferentıal cross sectıons at 5 0 GeV/c, (s = 11 31 GeV^2)

$\bar{t}$	dσ/dt(mb/GeV^2)	cos θ^*	$\bar{t}$	dσ/dt (mb/GeV^2)	cos θ^*
0.134	(0 346 ± 0 016) E + 02	0 966	0 506	(0 251 ± 0.020) E + 01	0 870
0 145	(0 320 ± 0 009) E + 02	0 963	0 547	(0.171 ± 0.028) E + 01	0.860
0.160	(0.280 ± 0 008) E + 02	0.959	0.603	(0 118 ± 0.004) E + 01	0.845
0.175	(0 239 ± 0.007) E + 02	0 955	0.699	(0 718 ± 0 023) E + 00	0 820
0.190	(0.201 ± 0 006) E + 02	0 951	0 797	(0 443 ± 0.015) E + 00	0 795
0 205	(0 179 ± 0.005) E + 02	0.947	0.896	(0 279 ± 0.011) E + 00	0.770
0 220	(0.170 ± 0 005) E + 02	0 943	0 996	(0.201 ± 0 008) E + 00	0.744
0 235	(0 148 ± 0 005) E + 02	0.940	1 10	(0 149 ± 0.007) E + 00	0 718
0.251	(0.133 ± 0 004) E + 02	0 935	1 20	(0 110 ± 0.006) E + 00	0 693
0.270	(0 118 ± 0 004) E + 02	0 931	1 30	(0.908 ± 0 050) E – 01	0 666
0.290	(0 960 ± 0.031) E + 01	0.926	1.40	(0.653 ± 0 043) E – 01	0 641
0 310	(0.812 ± 0 029) E + 01	0.920	1 49	(0 461 ± 0.037) E – 01	0.616
0 330	(0 701 ± 0 027) E + 01	0.915	1.64	(0 366 ± 0.026) E – 01	0 577
0 350	(0.633 ± 0 025) E + 01	0 910	2.32	(0.135 ± 0 013) E – 01	0 403
0.370	(0 538 ± 0 022) E + 01	0 905	2 76	(0 702 ± 0.110) E – 02	0 290
0.390	(0 489 ± 0.022) E + 01	0 900	3 12	(0.580 ± 0 170) E – 02	0 199
0.414	(0 406 ± 0 017) E + 01	0.894	5 28	(0 428 ± 0 104) E – 02	–0 357
0.444	(0.339 ± 0 017) E + 01	0 886	5 74	(0.430 ± 0.080) E – 02	–0 476
0.475	(0.288 ± 0 018) E + 01	0 878	6 27	(0 679 ± 0 256) E – 02	–0 611
			6 67	(0.141 ± 0 080) E – 01	–0 714

Table 3
Dıfferentıal cross sectıons at 6.0 GeV/c, (s = 13.16 GeV^2)

$\bar{t}$	dσ/dt(mb/GeV^2)	cos θ^*	$\bar{t}$	dσ/dt(mb/GeV^2)	cos θ^*
0 134	(0.290 ± 0 014) E + 02	0 972	0.608	(0.823 ± 0.032) E + 00	0 874
0 145	(0.270 ± 0.006) E + 02	0 970	0.701	(0 561 ± 0 021) E + 00	0 855
0.160	(0 239 ± 0.005) E + 02	0 967	0 799	(0.317 ± 0 010) E + 00	0 834
0 175	(0 222 ± 0 005) E + 02	0.964	0.897	(0 210 ± 0.007) E + 00	0.814
0 190	(0 191 ± 0.004) E + 02	0 961	0 997	(0.129 ± 0 005) E + 00	0.793
0 205	(0 174 ± 0 004) E + 02	0.957	1 10	(0 837 ± 0 038) E – 01	0 772
0.220	(0.150 ± 0 004) E + 02	0 954	1 20	(0.619 ± 0 032) E – 01	0.751
0.235	(0 124 ± 0 003) E + 02	0.951	1.30	(0.468 ± 0.027) E – 01	0.731
0 251	(0 108 ± 0 003) E + 02	0.948	1 40	(0.316 ± 0.021) E – 01	0 710
0.270	(0.925 ± 0.023) E + 01	0.944	1.50	(0.256 ± 0.019) E – 01	0.689
0.290	(0.772 ± 0 021) E + 01	0.940	1.59	(0 207 ± 0.017) E – 01	0.669
0 310	(0.704 ± 0.020) E + 01	0.936	1.74	(0 159 ± 0.011) E – 01	0 638
0.329	(0 615 ± 0.019) E + 01	0 932	1.94	(0 128 ± 0 011) E – 01	0 597
0 349	(0.533 ± 0 019) E + 01	0 927	2.13	(0 973 ± 0.109) E – 02	0 557
0.370	(0.450 ± 0 017) E + 01	0.923	2 78	(0.569 ± 0 061) E – 02	0.422
0.390	(0 403 ± 0.016) E + 01	0.919	3.26	(0.379 ± 0.047) E – 02	0.323
0.414	(0.323 ± 0.012) E + 01	0 914	5.34	(0 817 ± 0.288) E – 03	–0 109
0 444	(0.280 ± 0.011) E + 01	0 908	5 79	(0 107 ± 0.033) E – 02	–0.203
0 474	(0 222 ± 0.010) E + 01	0.902	6.30	(0.108 ± 0.027) E – 02	–0 309
0.504	(0 173 ± 0 009) E + 01	0.895	6.76	(0.972 ± 0 195) E – 03	–0.403
0 539	(0.138 ± 0 007) E + 01	0.888	7 24	(0 159 ± 0.032) E – 02	–0 504
			7.71	(0.197 ± 0.065) E – 02	–0.600

Table 4
Differential cross sections at 7.0 GeV/c, (s = 15.02 GeV^2)

$\bar{t}$	$d\sigma/dt$ (mb/GeV^2)	$\cos\theta^*$	$\bar{t}$	$d\sigma/dt$(mb/GeV^2)	$\cos\theta^*$
0.134	(0.311 ± 0.008) E + 02	0.977	1.10	(0.621 ± 0.029) E − 01	0.809
0.145	(0.275 ± 0.005) E + 02	0.975	1.19	(0.440 ± 0.024) E − 01	0.792
0.160	(0.239 ± 0.005) E + 02	0.972	1.30	(0.297 ± 0.019) E − 01	0.774
0.175	(0.210 ± 0.004) E + 02	0.970	1.40	(0.243 ± 0.017) E − 01	0.757
0.190	(0.186 ± 0.004) E + 02	0.967	1.50	(0.163 ± 0.019) E − 01	0.739
0.205	(0.161 ± 0.003) E + 02	0.964	1.60	(0.132 ± 0.012) E − 01	0.722
0.220	(0.154 ± 0.003) E + 02	0.962	1.74	(0.902 ± 0.071) E − 02	0.696
0.235	(0.132 ± 0.003) E + 02	0.959	1.95	(0.742 ± 0.061) E − 02	0.661
0.251	(0.117 ± 0.003) E + 02	0.956	2.14	(0.512 ± 0.051) E − 02	0.628
0.270	(0.103 ± 0.002) E + 02	0.953	2.33	(0.429 ± 0.106) E − 02	0.595
0.290	(0.862 ± 0.021) E + 01	0.950	2.52	(0.334 ± 0.109) E − 02	0.562
0.310	(0.714 ± 0.019) E + 01	0.946	2.83	(0.265 ± 0.035) E − 02	0.508
0.330	(0.588 ± 0.017) E + 01	0.943	3.19	(0.201 ± 0.029) E − 02	0.445
0.350	(0.492 ± 0.015) E + 01	0.939	3.58	(0.153 ± 0.027) E − 02	0.376
0.370	(0.440 ± 0.014) E + 01	0.936	3.99	(0.949 ± 0.194) E − 03	0.306
0.389	(0.388 ± 0.013) E + 01	0.932	4.36	(0.699 ± 0.202) E − 03	0.242
0.415	(0.303 ± 0.009) E + 01	0.928	5.87	(0.233 ± 0.137) E − 03	−0.021
0.444	(0.258 ± 0.009) E + 01	0.923	6.26	(0.255 ± 0.099) E − 03	−0.090
0.475	(0.201 ± 0.008) E + 01	0.917	6.70	(0.214 ± 0.119) E − 03	−0.166
0.509	(0.170 ± 0.007) E + 01	0.911	7.28	(0.232 ± 0.093) E − 03	−0.268
0.553	(0.121 ± 0.005) E + 01	0.904	7.77	(0.277 ± 0.089) E − 03	−0.353
0.614	(0.771 ± 0.035) E + 00	0.893	8.27	(0.434 ± 0.115) E − 03	−0.440
0.700	(0.481 ± 0.014) E + 00	0.878	8.73	(0.643 ± 0.148) E − 03	−0.519
0.799	(0.254 ± 0.008) E + 00	0.861	9.28	(0.572 ± 0.192) E − 03	−0.616
0.898	(0.157 ± 0.005) E + 00	0.844	9.71	(0.147 ± 0.039) E − 02	−0.690
0.996	(0.100 ± 0.004) E + 00	0.827	10.29	(0.124 ± 0.068) E − 02	−0.790

(GeV/c)^2. At higher momenta, fig. 9 clearly shows the appearance of a shoulder in the cross sections at $|t| \sim 1.5$ (GeV/c)^2.

Tabulations of the differential cross sections are given in tables 2–9. In the tables, t_{av} is the average value of $|t|$ for all events in the interval t_{min} to t_{max}, and θ^* is the c.m. scattering angle.

7. Discussion and conclusions

This section is devoted to discussion and interpretation of the results. Results for the variation of the logarithmic slope with t are given and discussed in subsect. 7.1. Comparisons are made with proton-proton data and with the reggeized absorption model of Kane and Seidl [35] whenever possible throughout the section but particularly in subsects. 7.2 and 7.5. The behavior of the cross sections at 90° in the c.m.s.

Table 5
Differential cross sections at 8.0 GeV/c, (s = 16.88 GeV^2)

$\bar{t}$	$d\sigma/dt$(mb/GeV^2)	$\cos\theta^*$	$\bar{t}$	$d\sigma/dt$(mb/GeV^2)	$\cos\theta^*$
0.134	(0.313 ± 0.009) E + 02	0.980	1.30	(0.189 ± 0.013) E – 01	0.806
0.145	(0.264 ± 0.005) E + 02	0.978	1.40	(0.149 ± 0.011) E – 01	0.791
0.160	(0.219 ± 0.004) E + 02	0.976	1.50	(0.119 ± 0.010) E – 01	0.776
0.175	(0.187 ± 0.004) E + 02	0.974	1.60	(0.101 ± 0.009) E – 01	0.761
0.190	(0.169 ± 0.003) E + 02	0.972	1.74	(0.789 ± 0.057) E – 02	0.739
0.205	(0.151 ± 0.003) E + 02	0.969	1.95	(0.545 ± 0.048) E – 02	0.709
0.220	(0.132 ± 0.003) E + 02	0.967	2.14	(0.316 ± 0.034) E – 02	0.679
0.235	(0.116 ± 0.002) E + 02	0.965	2.34	(0.252 ± 0.030) E – 02	0.650
0.251	(0.987 ± 0.020) E + 01	0.962	2.54	(0.185 ± 0.027) E – 02	0.620
0.270	(0.856 ± 0.018) E + 01	0.960	3.20	(0.119 ± 0.021) E – 02	0.521
0.290	(0.761 ± 0.017) E + 01	0.957	3.58	(0.709 ± 0.139) E – 03	0.464
0.310	(0.651 ± 0.015) E + 01	0.954	3.98	(0.519 ± 0.115) E – 03	0.403
0.330	(0.578 ± 0.014) E + 01	0.951	4.36	(0.162 ± 0.063) E – 03	0.347
0.350	(0.486 ± 0.013) E + 01	0.948	4.78	(0.236 ± 0.072) E – 03	0.284
0.370	(0.395 ± 0.012) E + 01	0.945	5.21	(0.868 ± 0.406) E – 04	0.220
0.390	(0.341 ± 0.011) E + 01	0.942	5.66	(0.974 ± 0.572) E – 04	0.152
0.414	(0.281 ± 0.008) E + 01	0.938	6.42	(0.808 ± 0.429) E – 04	0.038
0.444	(0.217 ± 0.007) E + 01	0.933	6.68	(0.943 ± 0.303) E – 04	–0.001
0.474	(0.175 ± 0.006) E + 01	0.929	7.38	(0.425 ± 0.207) E – 04	–0.106
0.509	(0.134 ± 0.005) E + 01	0.924	7.79	(0.552 ± 0.237) E – 04	–0.167
0.552	(0.936 ± 0.037) E + 00	0.917	8.39	(0.420 ± 0.266) E – 04	–0.257
0.617	(0.646 ± 0.025) E + 00	0.908	8.74	(0.966 ± 0.428) E – 04	–0.308
0.698	(0.336 ± 0.015) E + 00	0.895	9.30	(0.159 ± 0.047) E – 03	–0.393
0.798	(0.169 ± 0.005) E + 00	0.880	9.74	(0.128 ± 0.042) E – 03	–0.459
0.897	(0.105 ± 0.004) E + 00	0.866	10.28	(0.232 ± 0.057) E – 03	–0.540
0.997	(0.606 ± 0.025) E – 01	0.851	10.77	(0.288 ± 0.080) E – 03	–0.613
1.10	(0.406 ± 0.020) E – 01	0.836	11.18	(0.336 ± 0.111) E – 03	–0.674
1.20	(0.255 ± 0.015) E – 01	0.821	11.77	(0.890 ± 0.314) E – 03	–0.763

is discussed in detail in subsect. 7.3. Comparisons are made with various theoretical parameterizations in subsect. 7.4. Our conclusions are summarized in subsect. 7.6.

7.1. Logarithmic slope

Traditionally elastic scattering data in the diffraction region has been parameterized by $d\sigma/dt = Ae^{Bt}$, with the interpretation that the logarithmic slope B is a measure of the interaction radius, $R = 2\sqrt{B}$. This parameterization adequately describes the data only if the fit is restricted to a small region in $|t|$, typically $0.2 \leqslant -t \leqslant 0.5$ (GeV/c)^2. Table 10 lists the values of fitted slopes along with corresponding radii for these data. The good statistics at small $|t|$ for the np data of this experiment made it possible to fit the logarithmic slope over small intervals in $|t|$. In fig. 12 is plotted the logarithmic slope parameter *versus* $|t|$. A steepening of the slope is seen at $|t| \sim$

Table 6
Differential cross sections at 9.0 GeV/c, (s = 18.74 GeV^2)

$-t$	$d\sigma/dt$ (mb/GeV^2)	cos θ^*	$-t$	$d\sigma/dt$ (mb/GeV^2)	cos θ^*
0.130	(0.292 ± 0.007) E + 02	0.983	0.553	(0.796 ± 0.029) E + 00	0.927
0.145	(0.252 ± 0.004) E + 02	0.981	0.615	(0.528 ± 0.019) E + 00	0.919
0.160	(0.214 ± 0.003) E + 02	0.979	0.694	(0.323 ± 0.016) E + 00	0.909
0.175	(0.176 ± 0.003) E + 02	0.977	0.796	(0.162 ± 0.008) E + 00	0.895
0.190	(0.152 ± 0.003) E + 02	0.975	0.898	(0.875 ± 0.032) E − 01	0.882
0.205	(0.131 ± 0.002) E + 02	0.973	0.995	(0.465 ± 0.020) E − 01	0.869
0.220	(0.120 ± 0.002) E + 02	0.971	1.10	(0.260 ± 0.014) E − 01	0.856
0.235	(0.104 ± 0.002) E + 02	0.969	1.20	(0.178 ± 0.011) E − 01	0.842
0.251	(0.970 ± 0.018) E + 01	0.967	1.30	(0.119 ± 0.009) E − 01	0.830
0.270	(0.793 ± 0.015) E + 01	0.965	1.40	(0.954 ± 0.079) E − 02	0.816
0.290	(0.687 ± 0.014) E + 01	0.962	1.50	(0.869 ± 0.075) E − 02	0.803
0.310	(0.555 ± 0.012) E + 01	0.959	1.60	(0.644 ± 0.065) E − 02	0.790
0.330	(0.482 ± 0.011) E + 01	0.957	1.75	(0.650 ± 0.046) E − 02	0.770
0.350	(0.418 ± 0.010) E + 01	0.954	1.95	(0.411 ± 0.035) E − 02	0.743
0.370	(0.373 ± 0.010) E + 01	0.951	2.15	(0.364 ± 0.034) E − 02	0.717
0.390	(0.323 ± 0.009) E + 01	0.949	2.34	(0.233 ± 0.027) E − 02	0.692
0.414	(0.269 ± 0.007) E + 01	0.946	2.55	(0.182 ± 0.027) E − 02	0.665
0.444	(0.206 ± 0.006) E + 01	0.942	2.74	(0.123 ± 0.021) E − 02	0.641
0.475	(0.162 ± 0.005) E + 01	0.938	2.93	(0.857 ± 0.210) E − 03	0.615
0.509	(0.121 ± 0.004) E + 01	0.933	3.22	(0.564 ± 0.116) E − 03	0.577
3.58	(0.320 ± 0.083) E − 03	0.530	9.26	(0.238 ± 0.107) E − 04	−0.217
3.95	(0.212 ± 0.059) E − 03	0.481	9.77	(0.217 ± 0.116) E − 04	−0.284
4.38	(0.159 ± 0.057) E − 03	0.424	10.25	(0.189 ± 0.145) E − 04	−0.347
5.11	(0.658 ± 0.221) E − 04	0.328	10.71	(0.339 ± 0.186) E − 04	−0.408
5.86	(0.283 ± 0.168) E − 04	0.230	11.31	(0.604 ± 0.232) E − 04	−0.487
6.78	(0.239 ± 0.168) E − 04	0.109	11.72	(0.880 ± 0.272) E − 04	−0.541
7.27	(0.271 ± 0.134) E − 04	0.045	12.28	(0.165 ± 0.042) E − 04	−0.614
7.62	(0.216 ± 0.112) E − 04	−0.002	12.74	(0.280 ± 0.072) E − 04	−0.674
8.26	(0.329 ± 0.135) E − 04	−0.086	13.26	(0.469 ± 0.145) E − 04	−0.743
8.75	(0.180 ± 0.098) E − 04	−0.150	13.67	(0.905 ± 0.400) E − 04	−0.797

0.18 (GeV/c)^2. These data along with the 10.4 GeV/c pp data from SLAC show that this small $|t|$ structure is not unique to ISR and Fermilab energies but is also present at lower energies.

The dashed curves in fig. 12 are the prediction of the reggeized absorption model of Kane and Seidl [35]. Their model describes the data reasonably well for $0.2 < -t < 1.5$ (GeV/c)^2, however it does not reproduce the slope increase shown by the data at smaller $|t|$.

Fig. 12 also shows that the slope gradually decreases with increasing $|t|$ until $|t| \simeq$ 1.5 (GeV/c)^2, after which it flattens out. At the higher momenta the data suggest a minimum in the slope near $|t|$ = 1.6 (GeV/c)^2. This corresponds to the shoulder in the differential cross sections for momenta above 7.0 GeV/c.

Table 7
Dıfferentıal cross sectıons at 10 0 GeV/c, (s = 20.61 GeV^2)

$\bar{t}$	$d\sigma/dt$ (mb/GeV^2)	$\cos\theta^*$	$\bar{t}$	$d\sigma/dt$ (mb/GeV^2)	$\cos\theta^*$
0 147	(0.242 ± 0.006) E + 02	0.983	0 616	(0 563 ± 0.018) E + 00	0 928
0.160	(0 218 ± 0.003) E + 02	0.981	0 694	(0 316 ± 0 015) E + 00	0 919
0 175	(0 187 ± 0.003) E + 02	0.980	0 778	(0 162 ± 0.012) E + 00	0 909
0.190	(0.163 ± 0 003) E + 02	0 978	0 905	(0 860 ± 0 051) E − 01	0 894
0.205	(0 145 ± 0.003) E + 02	0.976	0 999	(0 513 ± 0.033) E − 01	0 883
0 220	(0.123 ± 0.002) E + 02	0.974	1.10	(0 255 ± 0 015) E − 01	0.872
0 235	(0 109 ± 0.002) E + 02	0 973	1 20	(0 147 ± 0.011) E − 01	0 860
0 251	(0 923 ± 0.017) E + 01	0.971	1 30	(0.101 ± 0.008) E − 01	0.848
0 270	(0 766 ± 0 014) E + 01	0.968	1.40	(0 757 ± 0 073) E − 02	0 837
0 290	(0 686 ± 0 013) E + 01	0 966	1.50	(0 645 ± 0 065) E − 02	0 824
0.310	(0 580 ± 0 012) E + 01	0 964	1.60	(0 548 ± 0 058) E − 02	0 813
0 330	(0 496 ± 0.011) E + 01	0 961	1 74	(0.442 ± 0.038) E − 02	0 796
0 350	(0 409 ± 0 010) E + 01	0.959	1 94	(0 378 ± 0 033) E − 02	0.773
0 370	(0 356 ± 0 009) E + 01	0 957	2.14	(0 294 ± 0 028) E − 02	0 750
0.390	(0 307 ± 0 008) E + 01	0.954	2 35	(0 202 ± 0.022) E − 02	0 725
0 415	(0 246 ± 0 006) E + 01	0 951	2.55	(0 153 ± 0 029) E − 02	0 701
0.444	(0.206 ± 0 005) E + 01	0 948	2.76	(0 130 ± 0.030) E − 02	0.677
0.480	(0 155 ± 0 004) E + 01	0 944	2 94	(0 935 ± 0 235) E − 03	0 655
0 514	(0.131 ± 0.004) E + 01	0 940	3.25	(0 564 ± 0 147) E − 03	0 620
0.554	(0 869 ± 0.028) E + 00	0 935	3 60	(0 449 ± 0 080) E − 03	0 579
3 97	(0.205 ± 0.050) E − 03	0 536	10 73	(0 136 ± 0.072) E − 04	−0 256
4.48	(0 162 ± 0 046) E − 03	0 476	11 24	(0.146 ± 0 109) E − 04	−0 316
4.80	(0.657 ± 0 273) E − 04	0 438	11 74	(0 234 ± 0 128) E − 04	−0 375
5 21	(0 683 ± 0 263) E − 04	0 390	12.27	(0 331 ± 0.187) E − 04	−0 436
5.60	(0 243 ± 0 150) E − 04	0 344	12 81	(0 448 ± 0.182) E − 04	−0 499
7 55	(0.959 ± 0.626) E − 04	0 117	13 26	(0 374 ± 0.175) E − 05	−0.552
8 17	(0 104 ± 0 070) E − 04	0 043	13 78	(0.889 ± 0 257) E − 04	−0 614
8.70	(0 660 ± 0.520) E − 05	−0 019	14 29	(0 199 ± 0 048) E − 03	−0 673
9.20	(0.141 ± 0 076) E − 04	−0.077	14 76	(0.368 ± 0 091) E − 03	−0 728
9 69	(0 998 ± 0 609) E − 05	−0 134	15 23	(0 539 ± 0 168) E − 03	−0 783
10 21	(0.107 ± 0 063) E − 04	−0 195	15 68	(0 134 ± 0 142) E − 02	−0 836

7 2. Comparison wıth proton-proton data

On the basıs of earlıer experıments wıth generally poorer statıstics, some authors have argued that the np and pp cross sections appear virtually the same for all $|t|$ out to 90°. A vivıd way to ıllustrate the differences and similarities ın np and pp cross sections ıs shown in fig. 13. The ratio,

$$R \equiv \frac{d\sigma}{dt}(\mathrm{np}) \Big/ \frac{d\sigma}{dt}(\mathrm{pp}) ,$$

calculated poınt-by-poınt from the np data from thıs experiment and pp data of

Table 8
Dıfferentıal cross sectıons at 11.0 GeV/c, (s = 22 48 GeV^2)

$\bar{t}$	$d\sigma/dt$ (mb/GeV^2)	cos θ^*	$\bar{t}$	$d\sigma/dt$ (mb/GeV^2)	cos θ^*
0 175	(0 182 ± 0 003) E + 02	0.982	1 59	(0.613 ± 0 088) E − 02	0.832
0.190	(0 152 ± 0 003) E + 02	0 980	1.75	(0.483 ± 0.053) E − 02	0 816
0.205	(0 134 ± 0 002) E + 02	0 978	1 95	(0 432 ± 0.053) E − 02	0.794
0.220	(0.120 ± 0.002) E + 02	0.977	2 13	(0.249 ± 0 039) E − 02	0 775
0.235	(0.107 ± 0 002) E + 02	0 975	2 34	(0.223 ± 0.037) E − 02	0 753
0.251	(0.874 ± 0 016) E + 01	0 974	2.55	(0.146 ± 0 030) E − 02	0 731
0.270	(0.733 ± 0.014) E + 01	0.972	2 74	(0.112 ± 0 027) E − 02	0.710
0.290	(0 635 ± 0.013) E + 01	0 969	2 98	(0 817 ± 0 196) E − 03	0.686
0.310	(0 509 ± 0 011) E + 01	0 967	3.28	(0.474 ± 0 129) E − 03	0 654
0.330	(0.439 ± 0.010) E + 01	0 965	3.59	(0.363 ± 0.081) E − 03	0 621
0.350	(0 386 ± 0 009) E + 01	0.963	3 97	(0.235 ± 0.061) E − 03	0.581
0.370	(0 337 ± 0 009) E + 01	0 961	4.40	(0.182 ± 0 048) E − 03	0.536
0.390	(0 282 ± 0 008) E + 01	0 959	4.82	(0 925 ± 0 321) E − 04	0.491
0 415	(0 236 ± 0 006) E + 01	0 956	5 28	(0 511 ± 0 214) E − 04	0.443
0.444	(0.184 ± 0 005) E + 01	0 953	6.26	(0 179 ± 0 076) E − 04	0.339
0.475	(0 142 ± 0 005) E + 01	0.950	7.79	(0.831 ± 0.855) E − 05	0.178
0.509	(0 114 ± 0 004) E + 01	0 946	8.53	(0.531 ± 0.343) E − 05	0.100
0.554	(0.832 ± 0 027) E + 00	0 942	9 52	(0 710 ± 0.752) E − 05	−0.004
0.618	(0 510 ± 0 017) E + 00	0.935	10.59	(0.448 ± 0 273) E − 05	−0.118
0.695	(0.277 ± 0 014) E + 00	0.927	11 46	(0 633 ± 0.336) E − 05	−0.209
0.778	(0 158 ± 0.012) E + 00	0 918	12.36	(0 903 ± 0.459) E − 05	−0 304
1.01	(0.455 ± 0 053) E − 01	0 894	13 63	(0 144 ± 0 076) E − 04	−0.438
1 10	(0 269 ± 0.024) E − 01	0 884	14.44	(0.161 ± 0 072) E − 04	−0.523
1 20	(0.166 ± 0 016) E − 01	0 874	15.56	(0 441 ± 0.129) E − 04	−0 642
1 29	(0.115 ± 0 013) E − 01	0.864	16.24	(0.117 ± 0.045) E − 03	−0 714
1 40	(0.844 ± 0 105) E − 02	0.852	16 72	(0.191 ± 0.073) E − 03	−0 764
1.50	(0.574 ± 0 088) E − 02	0 842	17 17	(0.258 ± 0.148) E − 03	−0.812

Allaby et al. [8] at 10 GeV/c ıs plotted as a functıon of $|t|$. Even wıth the uncertaintıes ~ 10% ın absolute normalızation, it can be seen that the two cross sections are about equal only for $|t| \leqslant 0.8$(GeV/c)^2. For $0.8 \lesssim -t \lesssim 1.4$ (GeV/c)^2 the ratıo falls rapıdly and then levels off wıth the np cross section at about 50% of the pp until $|t| \sim 5.0$ (GeV/c)^2. At thıs point the np cross section seems to drop again to about 30% of the pp cross section. Its not clear what conclusions can be drawn from these data except that the np and pp differentıal cross sectıons differ quantitatively but are sımılar in shape. The dashed curve in fig. 13 is the predıction of the reggeized absorptıon model of Kane and Seidl [35]. Their model is able to account qualıtatıvely for the observed t-dependence of the np/pp ratıo only for $|t| \lesssim 1.0$ (GeV/c)^2.

Table 9
Differential cross sections at 12 0 GeV/c, (s = 24.35 GeV^2)

$\bar{t}$	$d\sigma/dt$ (mb/GeV^2)	$\cos\theta^*$	$\bar{t}$	$d\sigma/dt$ (mb/GeV^2)	$\cos\theta^*$
0.175	(0 163 ± 0 009) E + 02	0 983	1.74	(0.439 ± 0 070) E − 02	0 833
0 190	(0 143 ± 0 008) E + 02	0 982	1.93	(0 302 ± 0 060) E − 02	0 814
0.203	(0.140 ± 0 006) E + 02	0.981	2 14	(0 234 ± 0 049) E − 02	0 795
0 220	(0 115 ± 0.003) E + 02	0.979	2 33	(0 122 ± 0 036) E − 02	0 776
0 235	(0 104 ± 0 003) E + 02	0.977	2 54	(0 945 ± 0 307) E − 03	0 756
0 251	(0 898 ± 0 022) E + 01	0 976	2.74	(0.703 ± 0.263) E − 03	0.736
0 270	(0 780 ± 0 019) E + 01	0 974	2 94	(0 598 ± 0 277) E − 03	0.718
0 290	(0 679 ± 0.018) E + 01	0 972	3.66	(0 332 ± 0 112) E − 03	0 649
0 310	(0.551 ± 0.016) E + 01	0.970	3 99	(0 285 ± 0 078) E − 03	0 617
0.330	(0 446 ± 0 014) E + 01	0 968	4.39	(0 141 ± 0 057) E − 03	0 579
0 350	(0 377 ± 0 012) E + 01	0 966	4.81	(0 153 ± 0 057) E − 03	0.538
0 370	(0 331 ± 0 012) E + 01	0 965	5 21	(0 473 ± 0 264) E − 04	0 500
0 389	(0 256 ± 0 010) E + 01	0 963	5.93	(0 220 ± 0 172) E − 04	0 430
0.414	(0.215 ± 0 007) E + 01	0 960	6.49	(0 102 ± 0.089) E − 04	0 377
0 444	(0 167 ± 0.007) E + 01	0 957	7.67	(0 579 ± 0 723) E − 05	0.263
0 475	(0 135 ± 0 006) E + 01	0 954	9.59	(0.498 ± 0 498) E − 05	0 079
0.507	(0.101 ± 0 005) E + 01	0 951	10 30	(0 485 ± 0 317) E − 05	0.002
0.553	(0 701 ± 0.034) E + 00	0 947	11 58	(0 352 ± 0.403) E − 05	−0 112
0 617	(0 398 ± 0.021) E + 00	0 941	12 57	(0 380 ± 0 380) E − 05	−0 207
0.696	(0 255 ± 0 019) E + 00	0.933	13 45	(0 744 ± 0 526) E − 05	−0 292
0 782	(0 142 ± 0.017) E + 00	0 925	14.59	(0.689 ± 0 689) E − 05	−0 401
1 18	(0 235 ± 0 082) E − 01	0 893	15 44	(0 126 ± 0 073) E − 04	−0 483
1 21	(0 170 ± 0.040) E − 01	0 884	16 52	(0.134 ± 0 106) E − 04	−0 587
1 31	(0.114 ± 0 023) E − 01	0.875	17 43	(0 247 ± 0 148) E − 04	−0.674
1 40	(0.668 ± 0 137) E − 02	0 866	18 29	(0 109 ± 0 062) E − 03	−0 757
1 50	(0 628 ± 0 128) E − 02	0 856	18.78	(0.232 ± 0 132) E − 03	−0 804
1.60	(0 387 ± 0.097) E − 02	0.847	19 20	(0 712 ± 0 345) E − 03	−0 844

7.3. Cross sections at 90°

The values of the cross sections at 90° in the c.m.s. are listed in table 11. To compare these data with 90° proton-proton data, table 11 also lists the np/pp ratio calculated from these data and pp data of Akerlof et al. [14]. In fig. 14 the ratio is plotted *versus* incident momentum. The data are consistent with R being independent of momentum. The average ratio is $\bar{R}$ = 0.34 ± 0.05 over the momentum range 5 to 12 GeV/c. Also plotted in fig. 14 are lower energy ratios calculated using data of Perl et al. [4] and Kammerud et al. [9]. The predictions of various models are indicated by the dashed lines. These data rule out the model of Fishbane and Quigg [21] and the statistical model [26] and also seem inconsistent with that of Wu and Yang [29], (see sect. 3). The ratios are close to the charge symmetry limit.

The errors make it difficult to determine the angle at which $d\sigma/dt$ is a minimum

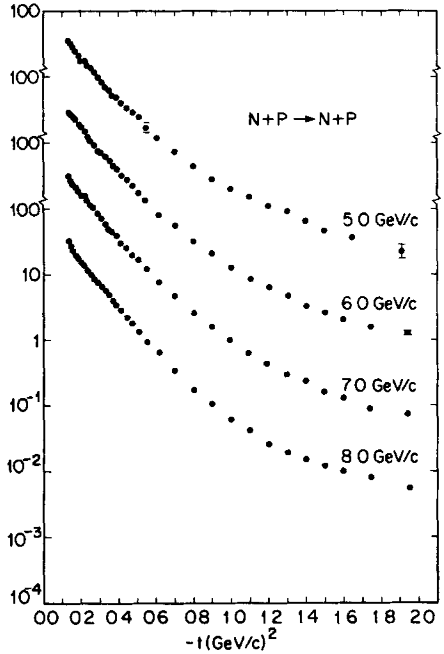

Fig 10. Neutron-proton elastic differential cross sections from 5 to 8 GeV/c for $|t| < 2$ (GeV/c)^2

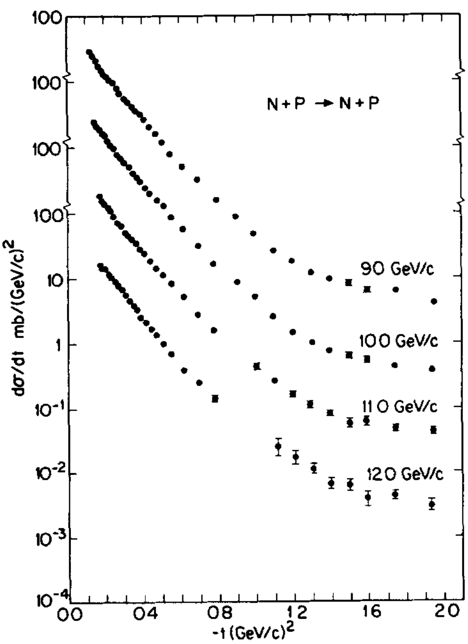

Fig. 11. Neutron-proton elastic differential cross sections from 9 to 12 GeV/c for $|t| < 2$ (GeV/c)^2.

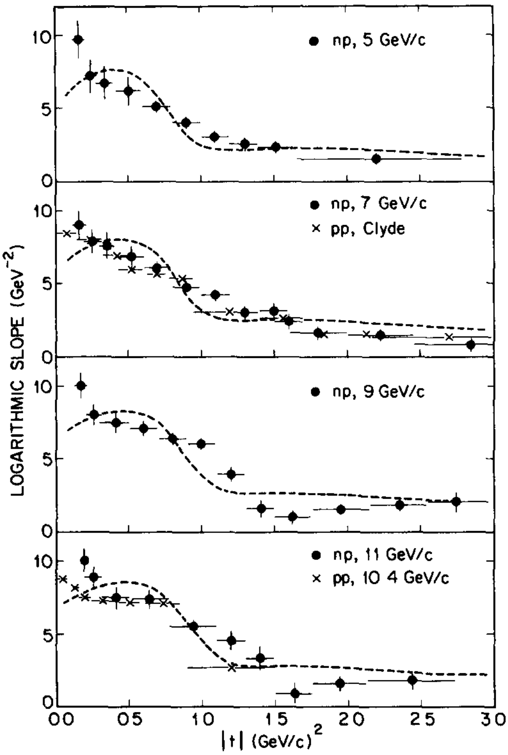

Fig 12 The t-dependence of the logarithmic slope for np and pp elastic scattering The dashed curve is the prediction of the reggeized absorption model of Kane and Seidl [35]

Table 10
Slopes of the diffraction peak for neutron-proton elastic scattering for $0.2 < -t < 0\ 5\ (\mathrm{GeV}/c)^2$

P (GeV/c)	B ((GeV/c)$^{-2}$)	R (fm)
5 0	7.10 ± 0.12	1.05
6 0	7 54 ± 0.10	1.08
7 0	7.87 ± 0 08	1 105
8 0	7 90 ± 0 08	1 107
9 0	7 80 ± 0.07	1.10
10.0	7 99 ± 0 07	1 11
11 0	8.26 ± 0.07	1.13
12 0	8.66 ± 0.10	1 16

$\frac{d\sigma}{dt} = Ae^{Bt}$, $\quad R = 2\sqrt{B}$

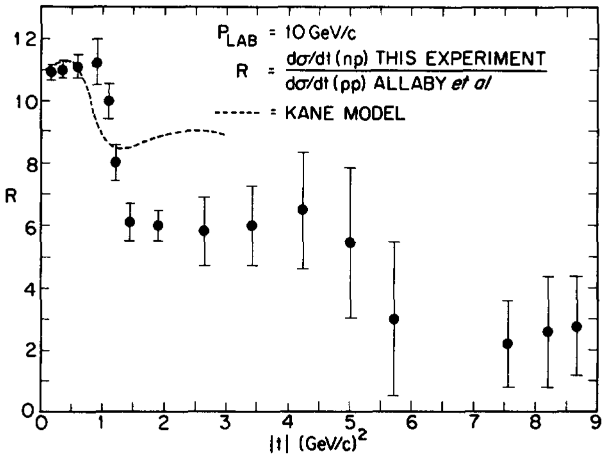

Fig. 13. The ratio of neutron-proton to proton-proton elastic differential cross sections at 10 GeV/c *versus* $|t|$.

but is appears to be near or just beyond 90°. The data are also consistent with the slope of $d\sigma/dt$ at 90° being zero.

The energy dependence of the 90° cross sections for neutron-proton and proton-proton data are plotted in fig. 15. Again the data of Perl et al. [4], Akerlof et al. [14], and Kammerud et al. [9] are included. A fit of the data with $s > 10$ GeV^2 to an s^{-n} dependence yielded $n = 10.40 \pm 0.34$ with χ^2/DF = 2.41 for the np data

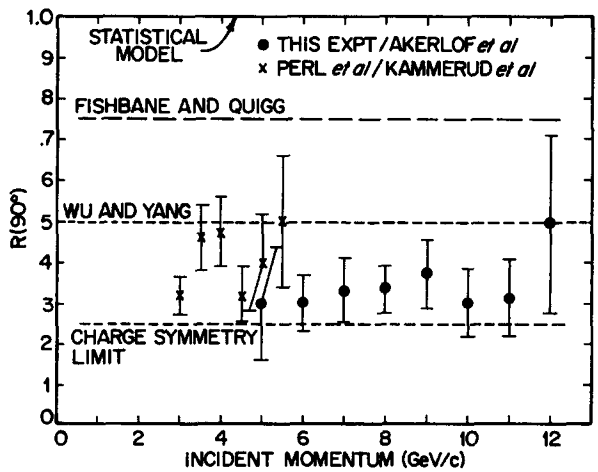

Fig. 14. Momentum dependence of the ratio of np to pp cross sections at 90° in the c.m.s The dashed lines are the predictions of various models.

Table 11
Neutron-proton cross sections at 90° cm

P (GeV/c)	$\sigma_{np}(90°)$ (μb/(GeV/c)^2)	$R = \sigma(np)/\sigma(pp)$ ($\theta^* = 90°$)
5 0	4.28 ± 1.0	0.29 ± 0 14
6 0	0.94 ± 0 22	0 30 ± 0.07
7 0	0.23 ± 0.054	0.33 ± 0 08
8.0	0.069 ± 0 012	0 34 ± 0 06
9.0	0 025 ± 0.0055	0.37 ± 0 08
10.0	0 01 ± 0 0028	0.29 ± 0 08
11 0	0 0058 ± 0 0018	0.31 ± 0 1
12 0	0.0043 ± 0 0019	0.50 ± 0 22

and $n = 9.81 \pm 0.05$ with χ^2/DF = 13.7 for the pp data. The dimensional counting rule of Brodsky and Farrar [17] predict $n = 10$ for both np and pp data at 90°. These data appear consistent with that prediction. However, if we fit our data at 60° and 120° to an $s^{-n(\theta^*)}$ dependence, we obtain $n(60°) = 8.04 \pm 0.15$ and $n(120°)$

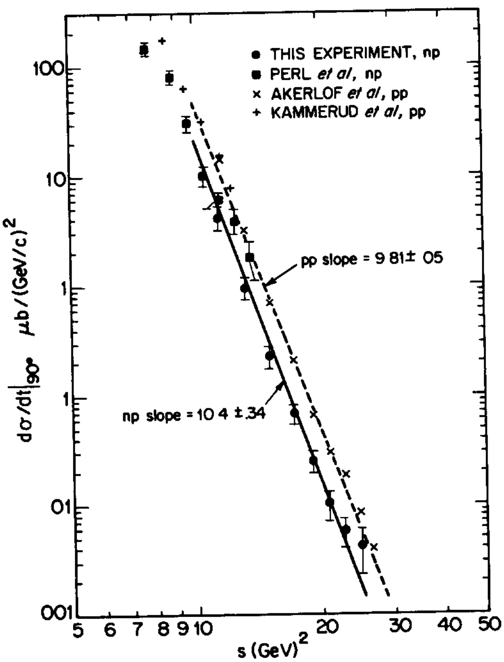

Fig. 15 Energy dependence of the 90° cross sections for neutron-proton and proton-proton data. The fitted slopes are consistent with the dimensional counting rule for $10 < s < 30$ GeV^2.

= 8.1 ± 0.22 Hence, our data show agreement with the dimensional counting rule only if θ^* is restricted to be close to 90°.

7.4. Angular dependence

To consider the question of the symmetry of $d\sigma/dt$ about 90° in the c m.s. it is convenient to examine the curves plotted in fig. 16. The solid line represents a smooth curve drawn through the 9 GeV/c data for $\theta^* \leqslant 90°$ The dashed line represents the data for $\theta^* \geqslant 90°$ but reflected about 90° to facilitate a direct angle for angle comparison Recall that eq. (5) (in subsect. 3.2) expressed the differential cross section in terms of pure $I = 0$ and $I = 1$ isospin amplitudes plus an interference term. Perfect symmetry of the np cross sections about 90° would imply no interference between these two amplitudes. Hence, the lack of symmetry of $d\sigma/dt$ about $\theta^* = \frac{1}{2}\pi$ is a test of the importance of the interference term in eq (5). Since the diffraction peak is so much larger than the backward charge exchange peak, there must be a strong interference in the amplitudes for θ^* close to 0°. From fig 16 it is apparent that symmetry breaks down at $|\cos\theta^*| \simeq 0.1$, so that there is also a significant interference of $I = 0$ and $I = 1$ amplitudes even at large θ^*.

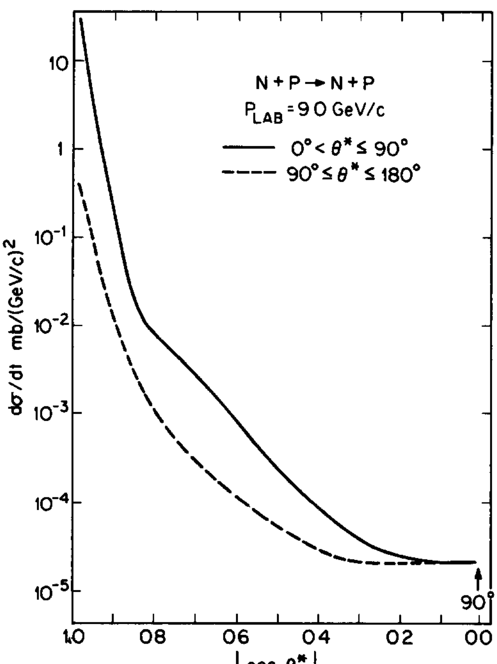

Fig 16 A smooth curve drawn through the neutron-proton data at 9 GeV/c and plotted *versus* $|\cos\theta^*|$ to test for symmetry about 90° in the c.m s

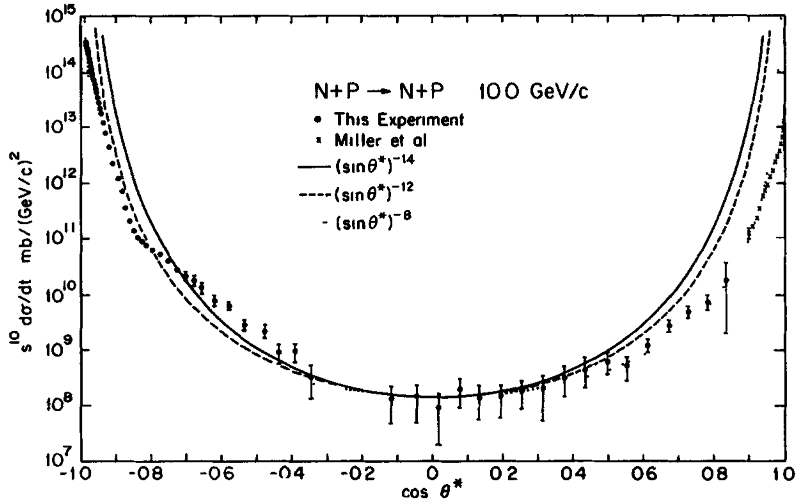

Fig. 17. Comparison of neutron-proton data at 10 GeV/c with angular dependence predictions for large-angle cross sections

Many models have been suggested to calculate or parameterize the angular dependence of the differential cross section for large values of θ^* The various results of these attempts are summarized in table 12. Entries (1)–(3) maintain the factorized form

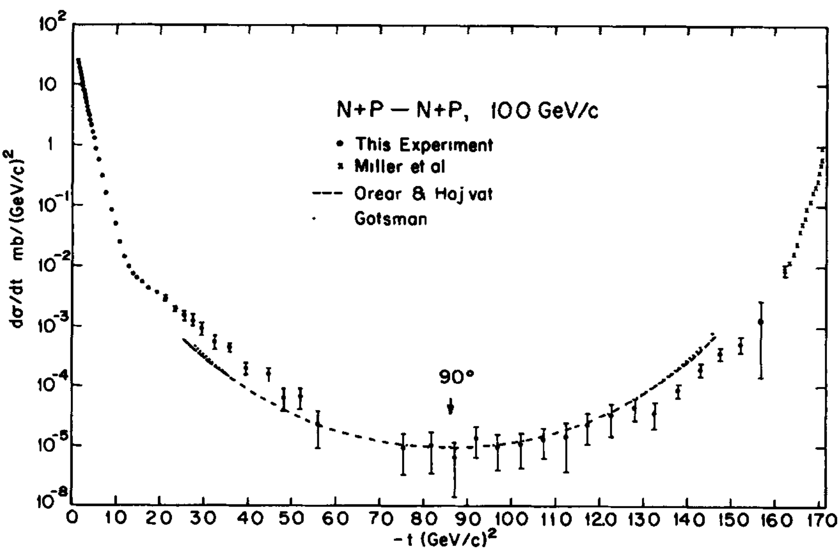

Fig. 18. Comparison of neutron-proton data at 10 GeV/c with large P_T parameterizations for differential cross sections.

Table 12
Predictions for the angular dependence of large angle neutron-proton cross sections

$f(\theta^*)$	Model	Authors and Ref
(1) $(\sin\theta^*)^{-12}$	CIM	Brodsky, Blankenbecler, Gunion [19]
(2) $(\sin\theta^*)^{-8}$	CIM and dimensional counting	Pire [23]
(3) $(\sin\theta^*)^{-14}$	Fit to pp data	Landshoff and Polkinghorne [22]
(4) $s^{-2}\,e^{-7P_T}$	Fit to pp data from the the ISR	Hojvat and Orear [24]
(5) $s^{-2}(P_T^2+m_V^2)^{-8}$ $m_V^2 = 0.71\ \mathrm{GeV}^2$	$(P_T)^{-1}$ as fundamental length in CIM	Gotsman [25]

suggested by eq. (2). Entries (4) and (5) introduce P_T as the relevant parameter and arrive at non-factorized parameterizations for the s and θ dependencies. The $f(\theta^*)$ from entries (1)–(3) are plotted *versus* $\cos\theta^*$ in fig. 17 and are compared with the 10 GeV/c data from this experiment. The parameterizations of entries (4)–(5) are plotted *versus* $|t|$ in fig. 18 and also compared with 10 GeV/c data. All the curves in these two figures have been normalized to agree with the data at 90° in the c.m.s. It is apparent that all the predictions are in reasonable agreement with the data for large t and u, or θ^* near 90°. However, away from the large-angle region all the predictions are equally inconsistent with the data.

7.5. *Small-angle parameterization*

The data are compared with the reggeized absorption model of Kane and Seidl [35] for several momenta in fig. 19. The curves in the figure are calculated according to the prescription of the authors using their published global parameters. This model describes the general features of the data quite well. However, it fails to account for some of the details. First, although the authors claim this model reproduces the small $|t|$ slope increase at high energies (ISR and Fermilab), it does not do so at lower energy. In fact, where the data turn upward for $t \lesssim 0.18$ (GeV/c)^2 the prediction has a downward curvature. Secondly, the model deviates from the data for $t > 1.0$ (GeV/c)^2 and does not give a good description of the shoulder in the data at $t \simeq 1.5$ (GeV/c)^2.

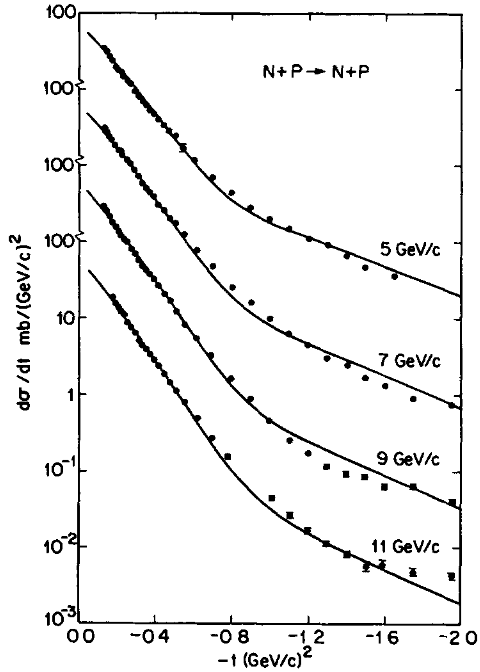

Fig. 19. Comparison of the neutron-proton cross sections with the reggeized absorption model of Kane and Seidl.

7.6. Conclusions

In this experiment neutron-proton differential cross sections were measured over a wide angular range for momenta between 5 and 12 GeV/c. The most interesting aspects of these measurements are summarized below.

(i) The small angle data at these energies show an increase in the logarithmic slope at $t \simeq 0.18$ (GeV/c)^2. This is the first time that this has been seen in np data.

(ii) A reggeized absorption model provides a good description of the small-angle data, but does not reproduce the change in slope at $|t| \simeq 0.18$ (GeV/c)^2 or the shoulder in the data near $|t| \simeq 1.6$.

(iii) At large angles the data exhibit a strong energy dependence as suggested by constituent models. Near 90° in the c.m.s. the observed s-dependence agrees well with the prediction of the dimensional counting rules of Brodsky and Farrar. However, the s-dependence at 60° and 120° does not agree with these rules.

(iv) The cross sections do not appear to be symmetric about 90° for $|\cos \theta^*| \gtrsim 0.1$.

(v) The angular dependence of the cross sections is still an open question theoretically. Several models with quite different assumptions produce similar results.

When compared to the data, all the models fail to reproduce the asymmetry about 90° observed in the data.

(vi) The observed ratio of neutron-proton to proton-proton cross sections at 90° in the c.m s in approximately $\frac{1}{3}$. There are no models which predict a ratio near this value.

(vii) The neutron-proton and proton-proton differential cross sections are quite different quantitatively, although their general behavior is similar.

We are greatly indebted to J Pluta and O Haas for their contributions in building much of the experimental apparatus. We would like to thank P Skubic, F. Ringia, C. DeHaven, and E. Martilla for their help in the various phases of installation and operation of the experiment. Our appreciation is extended to the entire ZGS staff and especially to B. Cork and R Klem for their assistance in making the experiment run as smoothly as possible We thank J. Luthe, A. Seidl, G. Kane, R. Cahn, and M Einhorn for many stimulating discussions about the experimental results. We especially wish to thank L W. Jones for his contributions to many phases of the experiment. We are indebted to Fermilab for the loan of the spectrometer magnet

References

[1] B.G Gibbard et al., Phys Rev. Lett 24 (1970) 22,
B.G. Gibbard et al., Nucl. Phys. B30 (1971) 77,
B G Gibbard, Ph D thesis, University of Michigan, 1970
[2] J. Engler et al., Phys Lett 29B (1969) 321,
J Engler et al , Nucl Phys. B62 (1973) 160
[3] V Bohmer et al., Nucl. Phys B91 (1975) 266
[4] M. Perl, J Cox, M.J. Longo and M.N Kreisler, Phys. Rev D1 (1970) 1857
M N Kreisler, Ph D. thesis, Stanford University 1966, SLAC report no SLAC-66,
M.N Kreisler et al , Phys Rev Lett 16 (1966) 1217.
[5] E.L. Miller et al., Phys. Rev. Lett 26 (1971) 984,
E L Miller, Ph D thesis, Ohio State University, 1971
[6] R.E. Mischke et al., Phys Rev. Lett 23 (1969) 542,
J L Friedes et al , Phys Rev Lett 15 (1965) 38,
G Manning et al , Nuovo Cim 41A (1966) 167,
M B Davis et al , Phys. Rev Lett 29 (1972) 139,
A Babaev et al , Nucl Phys B110 (1976) 189
[7] A R Clyde et al , Lawrence Radiation Laboratory report no UCRL-16275, unpublished
[8] J V Allaby et al , Phys Lett 28B (1968) 67,
J V. Allaby et al , Nucl Phys B52 (1973) 316
[9] R C Kammerud et al , Phys Rev D4 (1971) 1309
[10] C. Ankenbrandt et al , Phys. Rev 170 (1968) 1223
[11] C W. Akerlof et al., Phys. Lett. 59B (1975) 197,
A Bohm et al , Phys Lett. 49B (1974) 491,
H Dekkerret et al , Phys. Lett 62B (1976) 363.
[12] G. Barbiellini et al , Phys. Lett. 39B (1972) 663,
R K. Carnegie et al., Phys Lett 59B (1975) 313.

[13] R.A Carrigan, Jr., Phys Rev. Lett 24 (1970) 168.
[14] C.W Akerlof et al., Phys. Rev 159 (1967) 1138
[15] G. Giacomelli, Phys. Reports 23 (1976) 123,
H. Abarbanel, Rev Mod Phys 48 (1976) 435
[16] D Sivers, S J Brodsky and R Blankenbecler, Phys. Reports 23 (1976) 1, and references therein.
[17] S.J. Brodsky and G R Farrar, Phys. Rev Lett. 31 (1973) 1153
[18] V. Matveev et al, Nuovo Cim Lett 7 (1973) 719.
[19] R Blankenbecler and S. Brodsky, Phys Rev D10 (1974) 2973,
R. Blankenbecler, S. Brodsky and J. Gunion, Phys Lett 39B (1972) 649,
Phys Lett. 39B (1972) 649, 42B (1973) 461, Phys. Rev D6 (1972) 2652, D8 (1973) 4117, D10 (1974) 2153, D12 (1975) 3469.
[20] G Preparata, Nucl. Phys B80 (1974) 299, B89 (1975) 445.
[21] P. Fishbane and C Quigg, Nucl Phys B61 (1973) 469
[22] P V Landshoff and J C. Polkinghorne, Phys Lett 44B (1973) 293
[23] B. Pire, Nucl. Phys B114 (1976) 11
[24] C. Hojvat and J Orear, Cornell preprint CLNS-346 (October 1976)
[25] E Gotsman, Phys Rev. D15 (1977) 1302, Tel Aviv University preprint TAUP 572-76 (1976)
[26] R. Hagedorn, Nuovo Cim. Suppl 3 (1965) 147,
G. Fast, R Hagedorn and L W Jones, Nuovo Cim 27 (1963) 856,
E Fermi, Prog. Theor Phys 5 (1950) 570
[27] S. Frautschi, Nuovo Cim 12A (1972) 133.
[28] G. Eilam et al, Phys Rev D8 (1973) 2871.
[29] T T Wu and C N Yang, Phys. Rev 137 (1965) 708
[30] R Levi Setti, Elementary particles (University of Chicago Press, Chicago, 1963) 22
[31] M.J Longo et al, Nucl Instr. 95 (1971) 53.
[32] J.L. Stone, Ph D thesis, University of Michigan (Physics), 1977.
[33] P V.R Murthy, C A Ayre, H R. Gustafson, L W Jones and M J Longo, Nucl Phys B92 (1975) 269
[34] A.A Carter and D V. Bugg, Phys Lett 20 (1966) 203,
G. Beznogikh et al., Sov J. Nucl Phys. 18 (1974) 179.
[35] G.L. Kane and A. Seidl, Rev Mod. Phys 48 (1976) 309